

# Examination of hypotheses in the Kolmogorov refined turbulence theory through high-resolution simulations.

## Part 1. Velocity field

By LIAN-PING WANG<sup>1</sup>, SHIYI CHEN<sup>2</sup>,  
JAMES G. BRASSEUR<sup>3</sup> AND JOHN C. WYNGAARD<sup>4</sup>

<sup>1</sup>Department of Mechanical Engineering, 126 Spencer Laboratory, University of Delaware, Newark, DE 19716, USA

<sup>2</sup>IBM Research Division, T.J. Watson Research Center, PO Box 218, Yorktown Heights, NY 10598, USA

<sup>3</sup>Department of Mechanical Engineering, Pennsylvania State University, University Park, PA 16802, USA

<sup>4</sup>Department of Meteorology, Pennsylvania State University, University Park, PA 16802, USA

(Received 21 July 1994 and in revised form 2 October 1995)

The fundamental hypotheses underlying Kolmogorov–Oboukhov (1962) turbulence theory (K62) are examined *directly* and *quantitatively* by using high-resolution numerical turbulence fields. With the use of massively parallel Connection Machine-5, we have performed direct Navier–Stokes simulations (DNS) at  $512^3$  resolution with Taylor microscale Reynolds number up to 195. Three very different types of flow are considered: free-decaying turbulence, stationary turbulence forced at a few large scales, and a  $256^3$  large-eddy simulation (LES) flow field. Both the forced DNS and LES flow fields show realistic inertial-subrange dynamics. The Kolmogorov constant for the  $k^{-5/3}$  energy spectrum obtained from the  $512^3$  DNS flow is  $1.68 \pm 0.15$ . The probability distribution of the locally averaged dissipation rate  $\epsilon_r$  over a length scale  $r$  is nearly log-normal in the inertial subrange, but significant departures are observed for high-order moments. The intermittency parameter  $\mu$ , appearing in Kolmogorov's third hypothesis for the variance of the logarithmic dissipation, is found to be in the range of 0.20 to 0.28. The scaling exponents over both  $\epsilon_r$  and  $r$  for the conditionally averaged velocity increments  $\delta_r u | \epsilon_r$  are quantified, and the direction of their variations conforms with the refined similarity theory. The dimensionless averaged velocity increments  $(\overline{\delta_r u^n | \epsilon_r}) / (\epsilon_r r)^{n/3}$  are found to depend on the local Reynolds number  $Re_{\epsilon_r} = \epsilon_r^{1/3} r^{4/3} / \nu$  in a manner consistent with the refined similarity hypotheses. In the inertial subrange, the probability distribution of  $\delta_r u / (\epsilon_r r)^{1/3}$  is found to be universal. Because the local Reynolds number of K62,  $R_{\epsilon_r} = \epsilon_r^{1/3} r^{4/3} / \nu$ , spans a finite range at a given scale  $r$  as compared to a single value for the local Reynolds number  $R_r = \bar{\epsilon}^{1/3} r^{4/3} / \nu$  in Kolmogorov's (1941*a,b*) original theory (K41), the inertial range in the K62 context can be better realized than that in K41 for a given turbulence field at moderate Taylor microscale (global) Reynolds number  $R_\lambda$ . Consequently universal constants in the second refined similarity hypothesis can be determined quite accurately, showing a faster-than-exponential growth of the constants with order  $n$ . Finally, some consideration is given to the use of pseudo-dissipation in the context of the K62 theory where it is found that the probability distribution of locally averaged pseudo-dissipation  $\epsilon'_r$  deviates more from a log-normal model than the full dissipation

$\epsilon_r$ . The velocity increments conditioned on  $\epsilon'_r$  do not follow the refined similarity hypotheses to the same degree as those conditioned on  $\epsilon_r$ .

## 1. Introduction

In 1941, Kolmogorov published a statistical theory, known as the local similarity or universal equilibrium theory, of small-scale velocity fluctuations in high Reynolds number, incompressible, stationary turbulence (Kolmogorov 1941*a,b* referred to herein as K41). In this theory two fundamental hypotheses concerning fine-scale structure were made. The first hypothesis states that the small-scale motions (at scale  $r$  much less than the integral scale  $L$ ) are statistically isotropic and the distribution of the velocity difference  $[\mathbf{u}(x+r, t) - \mathbf{u}(x, t)]$  between two points in space is uniquely determined by a local length scale  $r \equiv |r|$ , the kinematic viscosity  $\nu$ , and the mean energy dissipation rate per unit mass

$$\bar{\epsilon} \equiv \overline{\frac{\nu}{2} \left( \frac{\partial u_i}{\partial x_j} + \frac{\partial u_j}{\partial x_i} \right) \left( \frac{\partial u_i}{\partial x_j} + \frac{\partial u_j}{\partial x_i} \right)},$$

where a bar above a quantity denotes an ensemble average. In particular, moments of longitudinal velocity increment,  $\delta_r u \equiv |u(x+r, y, z, t) - u(x, y, z, t)|$ , can be expressed as

$$\overline{(\delta_r u)^n} = (\bar{\epsilon} r)^{n/3} f_n(R_r), \quad (1.1)$$

where  $R_r = \bar{\epsilon}^{1/3} r^{4/3} / \nu = (r/\eta)^{4/3}$  is a local Reynolds number at scale  $r$  with local velocity scale  $(\bar{\epsilon} r)^{1/3}$ ,  $\eta = (\nu^3/\bar{\epsilon})^{1/4}$  being the Kolmogorov dissipation length scale. The functions  $f_n(R_r)$  are universal functions for flows at high Reynolds numbers,  $R_\lambda = \lambda u'/\nu$ ,  $\lambda$  and  $u'$  being the Taylor microscale and r.m.s. component velocity, respectively. Here  $R_\lambda$  can be viewed as a global Reynolds number for a given flow. More generally, the probability distribution of  $\delta_r u / (\bar{\epsilon} r)^{1/3}$  should only depend upon the local Reynolds number  $R_r$ . When  $n = 2$ , (1.1) implies that a universal energy spectrum  $E(k)$  exists at high wavenumbers under Kolmogorov scaling such that

$$\frac{E(k)}{(\bar{\epsilon} \nu^5)^{1/4}} = \Phi(k\eta) = (k\eta)^{-5/3} \phi(k\eta). \quad (1.2)$$

Kolmogorov's second similarity hypothesis states that when  $R_r \gg 1$  (i.e.  $r \gg \eta$  or  $k \ll \eta^{-1}$ ) the distribution of the normalized velocity increments  $\delta_r u / (\bar{\epsilon} r)^{1/3}$  becomes independent of  $\nu$ . It follows that in this *inertial subrange*,<sup>†</sup>

$$\overline{(\delta_r u)^n} = B_n (\bar{\epsilon} r)^{n/3}, \quad (1.3)$$

where  $B_n$  are universal constants. When  $n = 2$ , (1.3) implies the well-known inertial-

<sup>†</sup> Note, following Kraichnan (1974), we use the velocity increment  $\delta_r u$ , i.e. the magnitude of the velocity difference  $\Delta_r u \equiv u(x+r, y, z, t) - u(x, y, z, t)$  in stating Kolmogorov's theory. We feel that the velocity increment  $\delta_r u$  is a better quantity than the difference  $\Delta_r u$  as a measure of velocity scale since the latter can take both positive and negative values. The moments of even orders of  $\delta_r u$  are the same as those of  $\Delta_r u$ , but those of the odd orders differ. Traditionally the difference  $\Delta_r u$  has been used in stating K41 and there is an exact relation at the third order, i.e.  $\overline{(\Delta_r u)^3} = -\frac{4}{3} \bar{\epsilon} r$ . Recently, Stolovitzky & Sreenivasan (1993) have pointed out some similarity and differences between moments of the unconditioned  $\delta_r u$  and those of  $\Delta_r u$ . However we will show in §4 that the velocity increment  $\delta_r u$  rather than  $\Delta_r u$  should be used when studying Kolmogorov (1962) refined turbulence theory.

subrange energy spectrum,

$$E(k) = C_K \bar{\epsilon}^{2/3} k^{-5/3}, \quad (1.4)$$

where  $C_K$  is the Kolmogorov constant, and  $C_K = 0.76B_2$  (Monin & Yaglom 1975, p. 355).

While the  $k^{-5/3}$  spectrum is supported by numerous experimental measurements (e.g. Monin & Yaglom 1975, pp. 462–494), significant departures from the predicted scaling exponents of higher order moments of velocity differences ( $n > 2$ ) have been consistently observed (e.g. Kuo & Corrsin 1971; Anselmet *et al.* 1984). Furthermore, K41 predicts skewness and flatness of velocity derivatives to be universal constants at high global Reynolds number  $R_\lambda$ . Measurements indicate that skewness and flatness are a strong function of  $R_\lambda$  and, based on this observation, Wyngaard & Tennekes (1970) suggested that the normalized energy spectrum at high wavenumbers is not universal. This non-universality at dissipation-range  $k$  was later demonstrated by Champagne (1978) for  $R_\lambda$  in the range 40 to 13000. (Recently She *et al.* 1993 found that the energy spectra at various Reynolds numbers collapse when scaled by the wavenumber  $k_p$  of peak dissipation and by the spectrum level at  $k_p$ , suggesting a different, universal scaling may exist.) These departures from K41 have been attributed mostly to the existence of intermittent structure at small scales.

With ideas from Landau (see Landau & Lifshitz 1963) and Oboukhov (1962), Kolmogorov (1962) refined his original theory to take into account the spatial fluctuations in the turbulent energy dissipation rate  $\epsilon$  at scale  $r$  (referred to herein as K62). There are two aspects to the K62 refined theory. First, Kolmogorov assumed a log-normal distribution function for the dissipation rate volume-averaged over a sphere of diameter  $r$ ,

$$\epsilon_r(x, t) = \frac{6}{\pi r^3} \int_{|h| \leq r/2} \epsilon(x+h, t) dh, \quad (1.5)$$

and the variance of  $\ln \epsilon_r$  given by

$$\sigma_r^2 = A + \mu \ln\left(\frac{L}{r}\right), \quad (1.6)$$

where  $\mu$  is a universal constant,  $A$  is a constant depending on flow geometry, and  $L$  is an integral scale. Potential non-universality is introduced through  $A$  and  $L$ .

The second, more general, aspect of K62 is the refinement of the similarity hypotheses introduced in K41 by relating the moments of  $\delta_r u$  conditioned on  $\epsilon_r$  (Oboukhov 1962) to  $\epsilon_r$ ,  $r$ , and  $\nu$ , in a manner analogous to K41:

$$\overline{(\delta_r u)^n | \epsilon_r} = (\epsilon_r r)^{n/3} g_n(R_{\epsilon_r}), \quad \text{for } r \gg L, \quad (1.7)$$

where the ensemble average  $\overline{(\delta_r u)^n | \epsilon_r}$  is computed using those spatial points where  $\epsilon_r$  is at a given value, and  $g_n(R_{\epsilon_r})$  are hypothesized to be universal functions of a new local Reynolds number  $R_{\epsilon_r} = \epsilon_r^{1/3} r^{4/3} / \nu$ , with a velocity scale  $(\epsilon_r r)^{1/3}$  that varies at a fixed  $r$  with the volume-averaged dissipation rate  $\epsilon_r$ . A more general statement of this refined similarity hypothesis (RSH) is that the probability distribution of the normalized velocity difference

$$\beta \equiv \frac{\delta_r u}{(\epsilon_r r)^{1/3}}, \quad (1.8)$$

is a universal function of  $R_{\epsilon_r}$ .

The second similarity hypothesis of K41 is refined in K62 to state that when  $R_{\epsilon_r} \gg 1$ ,

$$\overline{(\delta_r u)^n | \epsilon_r} = D_n (\epsilon_r r)^{n/3}, \quad (1.9)$$

where  $D_n$  are universal constants, and the probability distribution of  $\beta$  takes a universal form independent of  $R_\epsilon$ .

Kolmogorov showed that, in the inertial range, the log-normal model for  $\epsilon_r$  leads to

$$\overline{(\delta_r u)^n} = F_n(A, L) \bar{\epsilon}^{n/3} r^{\zeta_n}, \quad (1.10)$$

where

$$\zeta_n = \frac{1}{3}n - \frac{1}{18}\mu n(n-3) \quad (1.11)$$

and potential effects of the outer scales are confined to the coefficients  $F_n$ . The second term in (1.11) indicates a departure from K41 of the scaling exponent of  $r$ . In particular, the  $k^{-5/3}$  inertial subrange of the energy spectrum becomes  $k^{-5/3-\mu/9}$ . Assuming  $\mu \sim O(1)$ , only a small correction is predicted in the scaling of the second moment. The correction can be quite large, however, for higher-order moments.

Many experimental measurements have been carried out to examine the validity of the log-normal model for the volume-averaged dissipation-rate fluctuations and to estimate the universal constant  $\mu$  in (1.6) (Gurvich & Yaglom 1967; Gibson, Stegun & McConnell 1970; Wyngaard & Pao 1972; Van Atta & Park 1972; Antonia, Statyaprakash & Hussain 1982; Anselmet *et al.* 1984; Praskovsky & Oncley 1994, to mention a few). In all these experiments, however, only the surrogate  $\epsilon' = 15\nu(\partial u/\partial x)^2$  is measured, with Taylor's frozen-field hypothesis, assuming that the local instantaneous dissipation rate is well approximated by an isotropic form which is strictly valid only in an ensemble-averaged sense. We shall return to this point later. The general finding from experiments is that the probability distribution of  $\epsilon'$  is close to log-normal except for the tails. Wyngaard & Tennekes (1970) showed that the skewness  $S$  and flatness  $K$  of the velocity derivatives are related by  $S \sim K^{3/8}$  if the log-normal model for  $\epsilon_r$  still applies as  $r \rightarrow 0$ . Their measurements appear to support this 3/8 scaling, suggesting that the log-normal model is reasonable for moments up to order 4. Experimentally, the measured values of  $\mu$  are in the range of 0.2 to 0.85, with a mean of about 0.5 in earlier measurements (Gurvich & Yaglom 1967; Gibson *et al.* 1970; Wyngaard & Pao 1972) and 0.2 in more recent measurements (Anselmet *et al.* 1984; Sreenivasan & Kailasnath 1993; Praskovsky & Oncley 1994).

On theoretical grounds, Gurvich & Yaglom (1967) showed that the log-normal distribution can be justified at very high Reynolds number under a scale-similarity hypothesis. Novikov (1970) and Mandelbrot (1974), however, have pointed out that the log-normal assumption cannot be strictly valid, especially for high-order moments. Kraichnan (1974) also pointed out that nonlinear cascade processes need not yield asymptotic log-normality. More recently, Liu (1993) developed an analysis for the probability distribution of the dissipation rate based on a nonlinear random differential equation for vorticity magnitude. He showed that the probability distribution can differ from log-normal in both asymptotic limits of very large and very small  $\epsilon$ . Other forms of probability distributions for  $\epsilon_r$ , such as log-stable (Kida 1991) and log-Poisson (She & Waymire 1995), have also been proposed. In the first part of the present paper we will examine the probability distributions of  $\epsilon$  and  $\epsilon_r$  for our numerically generated turbulence fields at various Reynolds numbers.

Experimental measurements of the scaling exponents  $\zeta_n$  in (1.10) have also been made (see Anselmet *et al.* 1984 and references therein) and the results agree reasonably well with the prediction (1.11) for  $n \leq 10$ . However, measurement of  $\zeta_n$  does not directly verify the refined similarity hypotheses, equations (1.7) and (1.9).

The second RSH, equation (1.9), relates purely inertial-range quantities  $\overline{(\delta_r u)^n}|_{\epsilon_r}$  to the dissipation rate averaged over an inertial-range scale, which allows one to link the

scaling property of the velocity increment directly to that of the dissipation rate. Thus the RSH, while never having been derived from first principles, has often been taken as a basis for developing theoretical models of high Reynolds number turbulence (Meneveau *et al.* 1990; Hosokawa 1991; She & Leveque 1994).

There has been a renewed interest in the validity of the RSH instigated by the work of Hosokawa & Yamamoto (1992), who found almost no correlation between the velocity increment  $\delta_r u$  and  $\epsilon_r$  in simulations of decaying isotropic turbulence at moderate Reynolds numbers, in direct conflict with the RSH. Later, Hosokawa & Yamamoto found their that their calculation was in error (see Chen *et al.* 1993). On the other hand, Praskovsky (1992) and Thoroddsen & Van Atta (1992) examined experimental data at high Reynolds numbers and found a significant correlation between  $\delta_r u$  and  $\epsilon'_r$ . In addition, Praskovsky (1992) showed that the conditionally averaged velocity increments,  $\delta_r u|_{\epsilon'_r}$ , depend on  $\epsilon'_r$ , although he did not quantify the relationship. Stolovitzky, Kailasnath & Sreenivasan (1992) also found a strong correlation between  $\delta_r u$  and  $\epsilon'_r$ , particularly for large  $\epsilon_r$  regions, in the atmospheric surface layer. Furthermore, they measured the probability distribution of the random variable  $\delta_r u|_{\epsilon'_r}/(\epsilon'_r r)^{1/3}$ . Stolovitzky & Sreenivasan (1994) noted that the velocity increment and  $\epsilon_r$  are both functionals of velocity gradient and thus they should be correlated in general. Stolovitzky & Sreenivasan also showed that a universal variable such as  $\beta$  in (1.8) exists for a fractional Brownian motion, implying that the RSH may apply to more general stochastic processes than Navier–Stokes turbulence.

A more detailed numerical analysis of  $\delta_r u|_{\epsilon'_r}$  in forced stationary and decaying isotropic turbulence over  $R_\lambda$  from 17 to 202 was carried out by Chen *et al.* (1993), using high-resolution direct numerical simulations. Chen *et al.* pointed out that a correlation between  $\delta_r u|_{\epsilon'_r}$  and  $\epsilon'_r$  must exist, independently of the Reynolds number, even in the absence of an inertial subrange. Specifically, as  $r/\eta \rightarrow 0$ , a Taylor expansion of the velocity leads to

$$\overline{\delta_r u^2|_{\epsilon'_r}} = \overline{\left(\frac{\partial u}{\partial x}\right)^2} r^2 = \frac{1}{15} \left(\frac{\epsilon'_r}{v}\right) r^2, \quad \overline{\delta_r u^2|_{\epsilon_r}} = \frac{1}{15} \left(\frac{\epsilon'_r|\epsilon_r}{v}\right) r^2 \approx \frac{1}{15} \left(\frac{\epsilon_r}{v}\right) r^2, \quad (1.12)$$

where the second relation cannot be rigorously derived but its validity will be shown numerically. Equation (1.12) is consistent with the first RSH, equation (1.7), with  $g_2 = R_{\epsilon_r}/15$ . More generally,

$$\overline{\delta_r u^n|_{\epsilon_r}} \sim \left(\frac{\epsilon_r}{v}\right)^{n/2} r^n \quad \text{for} \quad \frac{r}{\eta} \rightarrow 0. \quad (1.13)$$

Chen *et al.* (1993) focused on the scaling exponent of  $\epsilon'_r$  and showed, qualitatively, that the exponent changes from the prediction of (1.12) to that of the RSH (1.9) (with  $\epsilon_r$  replaced by  $\epsilon'_r$ ) as  $r$  increases.

The main focus of this study is the *quantitative* examination of the RSH by measuring the scaling exponents directly for various turbulence fields obtained from high-resolution (up to  $512^3$  grid points) simulations of isotropic turbulence. Because the direct numerical simulations resolve down to the Kolmogorov scale, their range of effective Reynolds numbers is necessarily limited. Whereas early direct simulations were restricted to lower resolutions that do not allow for a study of inertial-subrange dynamics, the current supercomputer architectures make it feasible to perform simulations for up to  $512^3$  grid points (Chen & Shan 1992; She *et al.* 1993). By forcing the lowest wavenumbers with a  $k^{-5/3}$  energy spectrum, it is possible to approximate an inertial subrange over a range of unforced scales spanning roughly a half a decade with  $512^3$  collocation points (Chen & Shan 1992; She *et al.* 1993).

We apply high-resolution ( $512^3$ ) direct simulations in the current study. In addition, we use one field in which the inertial range is extended through large-eddy simulation. Although the extent of the inertial subrange is still not large enough for a definitive study of the K62 theory, we shall show that the scaling exponents of the RSH proposed for very high Reynolds number can be partly realized in our high-resolution DNS flow fields by providing rather precise K62 inertial-subrange universal constants. Furthermore, we demonstrate that for a given global flow Reynolds number  $R_\lambda$ , the inertial subrange in the K62 context can be better resolved than the inertial subrange in the K41 context. This is because, at a given  $r$ , the local Reynolds number  $R_{\epsilon_r}$  spans a finite range as compared to a single value for the local Reynolds number  $R_r$  in the K41 context. In fact, we show that while the universal constant such as  $C_\kappa$  in (1.4) can only be approximately estimated from our high-resolution DNS turbulence fields, the universal constants in the K62 context, such as  $D_n$  in (1.9), can be very accurately determined from the same flow fields.

A major advantage of DNS over experiments is the easy access to the local dissipation rate in its exact form which, experimentally, requires very sophisticated measurement techniques (Wallace & Foss 1994; Tsinober, Kit & Dracos 1992). As mentioned earlier, all previous experimental studies approximate  $\epsilon_r$  in the K62 theory with the local one-dimensional surrogate  $\epsilon'_r$ . Tsinober *et al.* (1992) pointed out that, because the dissipation rate  $\epsilon$  is a quantity independent of the system of reference, it is best suited to describing physical processes. Both the instantaneous structure and the probability distribution of  $\epsilon$  are very different from  $\epsilon'$  (Narasimha 1990; Tsinober *et al.* 1992). An additional aim of this paper is to compare the statistics between  $\epsilon'_r$  and  $\epsilon_r$  in the context of the K62 theory (§5).

The paper is organized as follows. The general features of the isotropic, homogeneous turbulent flows from high-resolution simulations are presented and compared with experimental observations in §2. In §3 we examine the probability distribution of dissipation-rate fluctuations, as a function of both the spatial scale  $r$  and the local Reynolds number. We then study in §4 the RSH directly by quantifying the scaling exponents over both  $\epsilon_r$  and  $r$ , and we analyse the universal constants  $D_n$  in (1.9) and the probability distribution of  $\beta$ . Finally, the use of the pseudo-dissipation  $\epsilon'_r$  as a surrogate of the true dissipation is examined in §5 in the context of K62 theory. In addition, we consider throughout the paper the potential use of large-eddy simulation, in which the dissipation scales have been removed, to analyse the K62 theory in the inertial range of scales.

## 2. Analysis of the high-resolution simulations

In this section, we describe the various flow fields we use for the study of the K62 theory and their general features. The turbulence fields were generated by numerical simulation of the three-dimensional unsteady incompressible Navier–Stokes equations using a spectral code originally developed by Chen & Shan (1992) for the Connection Machine-2 (CM-2) but applied in this study on the more powerful, massively parallel CM-5 at Los Alamos National Laboratory. The large memory and built-in parallel algorithms of the CM-5 allowed for a  $512^3$  mesh resolution.

### 2.1. Flow simulation

The Navier–Stokes equations are solved on a cube of side  $L_B = 2\pi$  using a standard pseudospectral algorithm, with periodic boundary conditions in the three coordinate

Simulation	d512	d256c1	d256c2	f128	f256	f512	les256	Experiment <sup>†</sup>
Grid	512 <sup>3</sup>	256 <sup>3</sup>	256 <sup>3</sup>	128 <sup>3</sup>	256 <sup>3</sup>	512 <sup>3</sup>	256 <sup>3</sup>	—
Symbol	△	□	■	▽	○	●	◇	—
$u'$	0.121	0.676	0.256	0.856	0.855	0.889	0.856	17.5 → 8.5
$\bar{\epsilon}$	0.005264	0.1795	0.01381	0.2013	0.1768	0.2460	0.1856 <sup>‡</sup>	—
$\nu$	0.001377	0.001	0.001	0.004	0.002	0.001	0.000434 <sup>¶</sup>	—
$R_\lambda$	20.9	132	68.1	100	151	195	—	72
$k_{max}\eta$	6.38	1.04	1.98	1.44	1.76	1.92	—	—
$\frac{(\partial u/\partial x)^3}{(\partial u/\partial x)^{3/2}}$	-0.521	-0.509	-0.529	-0.504	-0.498	-0.545	—	-0.50
$\frac{(\partial u/\partial x)^4}{(\partial u/\partial x)^2}$	4.00	5.79	4.98	5.25	5.40	6.70	—	—
$\Delta$	0.0122	0.0245	0.0245	0.0490	0.0245	0.0122	0.0245	—
$\eta$	0.0265	0.00864	0.0164	0.0237	0.0146	0.00798	0.004581 <sup>¶</sup>	—
$\lambda$ <sup>  </sup>	0.239	0.196	0.266	0.468	0.352	0.220	—	0.66 → 1.13
$L_f$	0.610	1.072	1.049	1.53	1.514	1.412	1.470	—
$\bar{\epsilon}L_f/u'^3$	1.81	0.623	0.863	0.491	0.428	0.494	0.435	—
$\tau_\eta$	0.512	0.0746	0.269	0.141	0.106	0.0638	—	—
$T_e$	5.05	1.59	4.10	1.79	1.77	1.59	1.72	—
$t/T_e$	1.2	1.26	2.68	8.4	6.8	1.81	4.65	—
$r_D$	0.262	0.165	0.251	0.349	0.286	0.150	—	—
$r_E$	1.05	3.14	3.14	3.14	3.14	3.14	3.14	—
$r_F$	—	—	—	1.26	1.26	1.26	1.26	—
$\zeta^2^{1/2}/\bar{\epsilon}$ <sup>††</sup>	0.914	1.300	1.14	1.21	1.25	1.46	—	1.37
$S_\zeta$	2.67	5.22	4.31	4.12	4.76	5.97	—	2.41
$F_\zeta$	15.8	63.7	44.3	34.4	50.3	83.2	—	9.63
$\frac{\omega_i\omega_j s_{ij}}{\omega^2 s_{ij} s_{ij}^{1/2}}$	0.213	0.215	0.222	0.221	0.222	0.236	—	0.15

<sup>†</sup> From Tsinober *et al.* (1992). The values listed here are an average over four locations in their wind tunnel,  $x/M = 30, 38, 64, 90$  – where self-similar decay is believed to be established and streamwise velocity-derivative skewness is constant. For quantities varying definitely with the downstream location, the range is shown. The units are: [L]=cm; [T]=s.

<sup>‡</sup> This value is computed as the total energy flux across the filter cut-off.

<sup>¶</sup> These effective viscosity and Kolmogorov scales are discussed in §4.

<sup>||</sup> Computed based on the dissipation,  $\lambda = (15\nu u'^2/\epsilon)^{1/2} = \sqrt{15}u'\tau_k$ .

<sup>††</sup>  $\zeta \equiv \epsilon - \bar{\epsilon}$ ,  $S_\zeta$  and  $F_\zeta$  are the skewness and flatness factors of  $\zeta$ , respectively.

TABLE 1. Flow characteristics from the high-resolution simulations. Note that the symbols are used consistently throughout the paper.

directions. The flow cube is discretized uniformly into  $N^3$  grid points, which defines the wavenumber components in Fourier space as

$$k_j = \pm n_j(2\pi/L_B) = \pm n_j, \quad (2.1)$$

where  $n_j = 0, 1, \dots, N/2 - 1$  for  $j = 1, 2, 3$ . A small portion of the energy at higher wavenumbers,  $k > k_{max}$  with  $k_{max} = N\sqrt{2}/3$ , is truncated at each time step to reduce aliasing errors.

Table 1 lists all the different fields used in this study. Both freely decaying and forced stationary isotropic turbulence fields are simulated. The freely decaying flow

is generated either from an initial random field with a prescribed spectrum (d512) or from a previously developed forced stationary turbulence (d256c1 and d256c2). These field data were extracted after the flows reached an asymptotic decay, characterized by power law decreases in kinetic energy and dissipation rate. For the case d512, the initial energy spectrum is proportional to  $k^2$  for  $k \leq 6.5$  and to  $k^{-5/3}$  for  $k > 6.5$ ; the power-law energy decay exponent was found to be  $-1.47$ , in good agreement with values previously obtained by Lee & Reynolds (1985) and Yeung & Brasseur (1991) for similar conditions but at lower ( $128^3$ ) mesh resolution. The fields d256c1 and d256c2 are from the same simulation at two different times, based on an initially stationary field with a extensive forced  $k^{-5/3}$  energy spectrum. A relatively high flow Reynolds number was obtained in this way, with a power-law energy decay exponent of about  $-1.81$ .

The forced isotropic fields (f128, f256, and f512) are generated by maintaining constant total energy in each of the first two wavenumber shells ( $0.5 < k \leq 1.5$  and  $1.5 < k \leq 2.5$ ), with the energy ratio between the two shells consistent with  $k^{-5/3}$ . Forcing at the lowest wavenumbers generates a statistically stationary flow usually with a more extensive nominal  $k^{-5/3}$  inertial range and higher Reynolds number, than freely decaying turbulence. The forcing, however, introduces artifacts at the large-scale fluid motions which may affect the structure and internal similarity scaling near the forcing scales. Thus only wavenumber bands larger than these forced bands are used for the study of K62 theory later in this paper. Nevertheless, at this moment we cannot be completely sure of the extent to which the close-to- $k^{-5/3}$  region approximates true inertial-range structure.

The spatial resolution of a spectral simulation is often monitored by the value of  $k_{max}\eta$ , which should be greater than one for the smallest scales of the flow to be resolved (Eswaran & Pope 1988), where  $\eta \equiv (\nu^3/\bar{\epsilon})^{1/4}$  is the Kolmogorov microscale. This condition is satisfied for all the fields. The isotropic-decay d512 field was designed to be over-resolved at the small scales, with  $k_{max}\eta = 6.4$ , to study the K62 scaling at small  $r/\eta$ .

The Fourier coefficients of the flow velocity were advanced in time using a second-order Adams–Bashforth method for the nonlinear term and an exact integration for the viscous term (Chen & Shan 1992). The time step was chosen to ensure that the Courant number was 0.4 or less for numerical stability and accuracy (Eswaran & Pope 1988).

The inertial range in the DNS fields is necessarily very narrow because the maximum scale separation is limited by the grid resolution. To extend the inertial subrange, we also make use of a flow field (les256) generated by moving the smallest inertial scales to higher wavenumbers through large-eddy simulation (LES). We model the flow scales below the grid spacing (filter scale), using the subgrid scale (SGS) closure scheme of Métais & Lesier (1992). We also apply the same forcing method used for our DNSs to the first two wavenumber shells to maintain the energy in the resolved field of the LES, thus moving the large-scale side of the inertial range to the lowest possible wavenumbers.

## 2.2. Dependence of flow characteristics on Reynolds number

In table 1 we list statistical flow characteristics of the DNS and LES fields. The first 15 quantities shown in the table (from top to bottom) are, in arbitrary units: the r.m.s. component fluctuating velocity  $u'$ , the spatially averaged energy dissipation rate  $\bar{\epsilon}$ , kinematic viscosity  $\nu$ , Taylor microscale Reynolds number  $R_\lambda \equiv u'\lambda/\nu$ , the resolution parameter  $k_{max}\eta$ , longitudinal velocity-derivative skewness and flatness averaged over



three directions, grid spacing  $\Delta$ , Kolmogorov length scale  $\eta$ , the transverse Taylor microscale  $\lambda$ , the longitudinal integral length scale  $L_f$ , the dimensionless energy dissipation rate  $\bar{\epsilon}L_f/u^3$ , Kolmogorov time scale  $\tau_\eta \equiv (\nu/\bar{\epsilon})^{1/2}$ , the large-scale eddy turnover time  $T_e \equiv L_f/u'$ , and the total integration time relative to eddy turnover time  $t/T_e$ . The Reynolds number  $R_\lambda$  in our simulations varies from 21 to 195. Note that the velocity-derivative skewness is around  $-0.5$  and almost independent of flow Reynolds number while derivative flatness increases with the Reynolds number. Both observations agree with previous DNS studies (Kerr 1985) and experimental measurements (Van Atta & Antonia 1980; Tsinober *et al.* 1992). The integral length scale is computed from the three-dimensional energy spectrum  $E(k)$ :

$$L_f = \frac{\pi}{2u'^2} \int_0^\infty \frac{E(k)}{k} dk, \quad (2.2)$$

where the energy spectrum  $E(k)$  is defined in the standard manner such that

$$\frac{3}{2}u'^2 = \int_0^\infty E(k)dk. \quad (2.3)$$

The spectrum was calculated by dividing wavenumber space into  $N/2$  shells centred on radius  $k$  and with unit bin width  $\Delta k = 1$ , and then summing the modal kinetic energy in each shell. The spatially averaged dissipation rate  $\bar{\epsilon}$  is related to the energy spectrum  $E(k)$  by

$$\bar{\epsilon} \equiv 2\nu\overline{s_{ij}s_{ji}} = 2\nu \int_0^\infty k^2 E(k) dk, \quad (2.4)$$

where  $s_{ij} = \frac{1}{2}(\partial u_i/\partial x_j + \partial u_j/\partial x_i)$  is the local rate of strain and  $\epsilon = 2\nu s_{ij}s_{ji}$ .

The dimensionless energy dissipation  $\bar{\epsilon}L_f/u^3$  should be independent of  $R_\lambda$  at sufficiently high  $R_\lambda$ . Consistent with the grid turbulence data given in Sreenivasan (1984), table 1 shows that  $\bar{\epsilon}L_f/u^3$  decreases with  $R_\lambda$  for the three free-decaying fields and has a value of 0.62 for the largest Reynolds number field d256c1. This asymptotic value is in good quantitative agreement with a recent study by Jiménez *et al.* (1993), who find  $\bar{\epsilon}L_f/u^3 \sim 0.7$  for  $R_\lambda \gtrsim 90$  in DNS turbulence forced by negative viscosity at lowest wavenumbers. Sreenivasan (1984) found an asymptotic value of approximately one for  $R_\lambda \gtrsim 60$  in grid-turbulence measurements. The approach of  $\bar{\epsilon}L_f/u^3$  to an asymptotic value of order 1 at high  $R_\lambda$  is based on the premise that no direct energy transfer takes place between the largest inertial scales and the dissipative scales in equilibrium turbulence (K41). Consequently the rate of dissipation depends on the energy-dominated length and time scales. Although the premise of no direct large-small-scale energy transfer is supported by the equations of motion (Brasseur & Corrsin 1987), it is possible that the large-scale velocity and time scales are influenced by large-scale structure, including the shape of the energy spectrum at low wavenumbers. There is some evidence for this possibility from comparing  $\bar{\epsilon}L_f/u^3$  in the three forced DNS fields (f128, f256, and f512) with the higher- $R_\lambda$  freely decaying case (d256c1), where the energy spectra at low wavenumbers are quite different. In all the forced simulations  $\bar{\epsilon}L_f/u^3 \sim 0.42 - 0.49$ , whereas in the decaying simulation  $\bar{\epsilon}L_f/u^3 \sim 0.62$ . Furthermore, if  $\bar{\epsilon}$  is replaced by energy flux in the LES, we obtain a value of 0.435 for  $\bar{\epsilon}L_f/u^3$ , about the same as the forced DNS fields.

Figure 1(a) shows log-log plots of Kolmogorov scaled three-dimensional energy spectra for the various DNS fields pre-multiplied by  $k^{5/3}$  so that an inertial range would appear as region of zero slope at the Kolmogorov constant  $C_\kappa$ . Also shown with crosses are grid-turbulence data from table 3 of Comte-Bellot & Corrsin (1971)

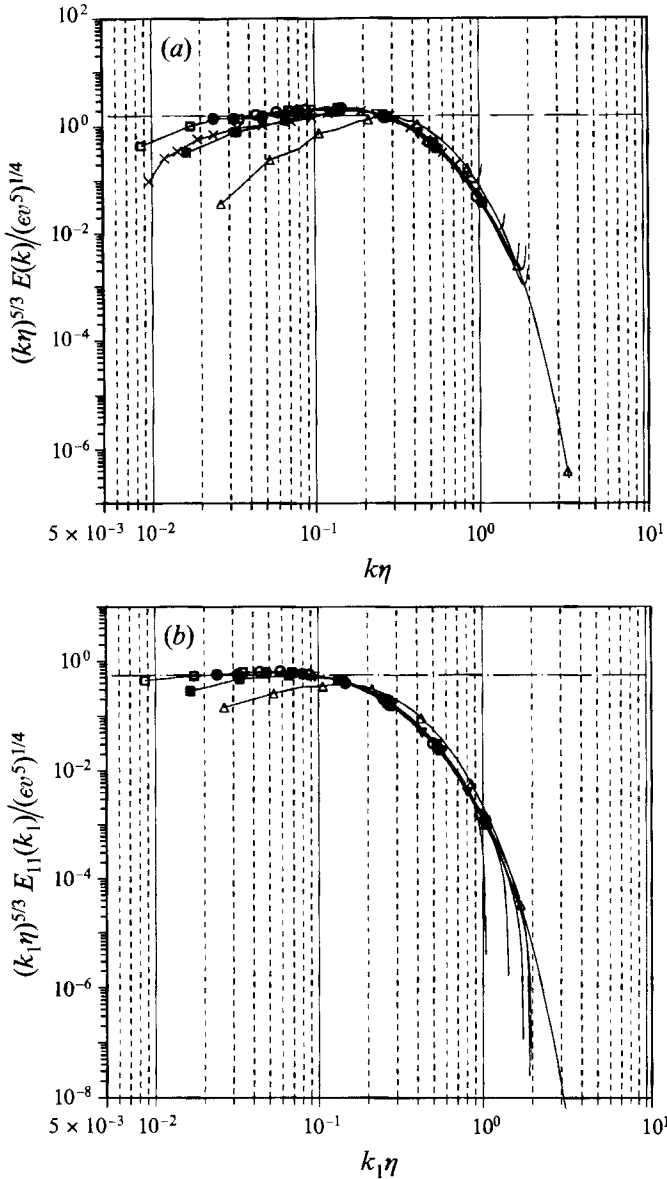


FIGURE 1. (a) The three-dimensional energy spectrum function  $E(k)$  and (b) the one-dimensional longitudinal energy spectrum  $E_{11}(k_1)$  for the simulated flows at various Taylor microscale Reynolds numbers using Kolmogorov scaling. For the forced turbulence fields, only the spectra for the unforced region  $k > 2$  or  $k_1 > 2$  are shown. The data taken from Comte-Bellot & Corrsin (1971) for a flow behind a 2-in grid at the location  $x/M = 98$  are plotted in (a) for comparison. The horizontal chain-dotted line marks the level of 1.6 in (a) and 0.53 in (b), the average Kolmogorov constant observed in experiments.  $\Delta$ ,  $512^3$ , free-decaying flow at  $Re_\lambda = 20.9$ ;  $\square$ ,  $256^3$ , free-decaying flow at  $Re_\lambda = 132$ ;  $\blacksquare$ ,  $256^3$ , free-decaying flow at  $Re_\lambda = 68.1$ ;  $\nabla$ ,  $128^3$ , forced stationary flow at  $Re_\lambda = 104$ ;  $\circ$ ,  $256^3$ , forced stationary flow at  $Re_\lambda = 151$ ;  $\bullet$ ,  $512^3$ , forced stationary flow at  $Re_\lambda = 195$ ;  $\times$ , Comte-Bellot & Corrsin (1971),  $Re_\lambda \approx 65$ . These symbols are used consistently throughout the paper and are shown in table 1.

(obtained by converting one-dimensional energy spectra) at  $U_{0t}/M = 98$ , where  $U$  is the mean velocity and  $M = 2$  inches is the grid width. Several observations can be made from this figure. First, with the exception of the very low- $R_\lambda$  d512 field, the energy spectra for different  $R_\lambda$  show a reasonably good collapse for  $k_{max}\eta > 0.1$  (roughly the peak in the dissipation-rate spectrum) under the Kolmogorov scaling, indicating self-similarity in the dissipation-range scales, consistent with the first K41 hypothesis, as described by equation (1.2). Second, the spectrum for the field d256c2 at  $R_\lambda = 68$  compares very well with the grid-turbulence data at  $R_\lambda \approx 65$  over all the wavenumber ranges. Third, as Reynolds number increases, the spectrum in the range  $0.01 < k_{max}\eta < 0.1$  gradually approaches the  $k^{-5/3}$  inertial range, with a Kolmogorov constant between 1.5 and 2 (as measured from the two forced DNS fields at  $256^3$  and  $512^3$  resolutions). This value for  $C_\kappa$  is in good agreement with the experimental value (Monin & Yaglom 1975, pp. 467–485).

To date it has been possible to experimentally measure only the one-dimensional energy spectra (e.g. Comte-Bellot & Corrsin 1971; Champagne 1978). In figure 1(b) we show the normalized one-dimensional energy spectra from the simulations, which are smoother than figure 1(a) due to the increased sampling at low wavenumbers and the averaging over the three directions. The collapse of data is even better than in figure 1(a), especially in the inertial range  $0.01 < k_{max}\eta < 0.1$ . This result is consistent with the observation of Monin & Yaglom (1975, pp. 356–358) that the inertial ranges for one-dimensional spectra extend to lower wavenumbers than for a three-dimensional spectrum. On the other hand, the viscous cut-off for the one-dimensional spectrum appears earlier than the three-dimensional spectrum. A more accurate estimate of the Kolmogorov constant can be made based on the One-dimensional spectra for the highest  $R_\lambda$  runs, f256 and f512; these give  $C_\kappa(1D) = 0.55 \pm 0.05$ , close to the average value of 0.53 obtained by Champagne (1978) by compiling various high Reynolds number experimental flows with  $R_\lambda \sim 138$  to 13000. Because  $C_\kappa = 55C_\kappa(1D)/18$  for an infinite inertial range (Monin & Yaglom 1975, p. 355),  $C_\kappa(1D) = 0.55 \pm 0.05$  corresponds to  $C_\kappa = 1.68 \pm 0.15$ . The observation that the Kolmogorov constant from our simulations agrees well with the experimental value obtained at much higher Reynolds numbers suggests that our numerically simulated inertial ranges, although very narrow, are representative of a true inertial range and we feel that  $C_\kappa \approx 1.68$  is an improvement over previous DNS values by Kerr (1990), Vincent & Meneguzzi (1991), and Jiménez *et al.* (1993). Recent measurements by Praskovsky & Oncley (1994) suggest that, at very high  $R_\lambda$ ,  $C_\kappa$  can depend on  $R_\lambda$  as  $C_\kappa \sim R_\lambda^{-\mu/2}$ , where the parameter  $\mu$  is introduced in equation (1.6).

Linear-linear plots for the normalized dissipation-rate spectra are shown in figure 2 for  $k\eta < 1$ . The data collapse well for the four fields with  $R_\lambda > 100$ , indicating that the Kolmogorov scaling (1.2) works well for moderately high Reynolds numbers. The normalized dissipation rate spectrum has a peak value of about 1.2 at  $k\eta \approx 0.16$ , in agreement with She *et al.* (1993) who found  $k\eta \approx 0.17$  at peak dissipation. As  $R_\lambda$  decreases below 100, the normalized spectrum shifts to higher  $k\eta$  and the peak magnitude decreases. The shift in peak dissipation rate to higher  $k\eta$  with decreasing  $R_\lambda$  can be understood in the following way. Let  $\xi \equiv k\eta$  and  $\Phi(\xi) = E(k)/(\bar{\epsilon}v^5)^{1/4}$ ; according to (2.4) we have

$$\int_0^\infty \xi^2 \Phi(\xi) d\xi = \frac{1}{2}, \quad (2.5)$$

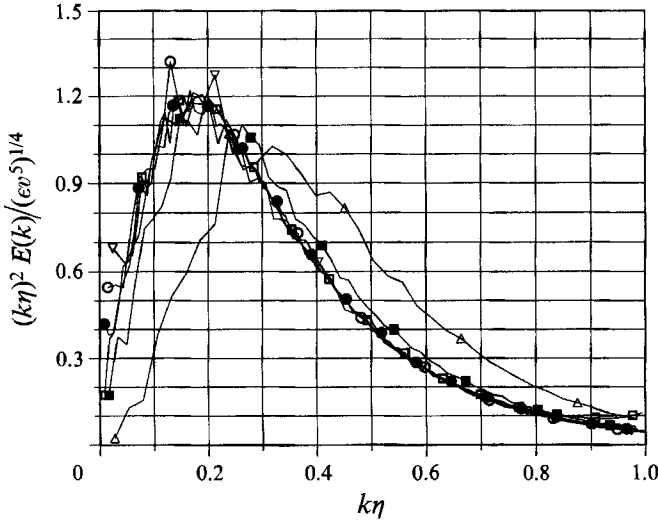


FIGURE 2. Linear-linear plots of the second moment of the three-dimensional energy spectrum.

so that the area under each curve in figure 2 is 0.5. In addition, equation (2.3) gives

$$\int_0^\infty \Phi(\xi) d\xi = \frac{3}{2} \left( \frac{u'}{v_k} \right)^2, \quad (2.6)$$

where  $v_k \equiv (\bar{\epsilon} v)^{1/4}$  is the Kolmogorov velocity scale. Because the separation in velocity scales,  $u'/v_k$ , decreases with decreasing Reynolds number, so does the integral of the normalized spectrum  $\Phi(\xi)$  according to (2.6). Because this integral is mainly determined by the low- $\xi$  region, the function  $\xi^2 \Phi(\xi)$  at low  $\xi$  also decreases with decreasing Reynolds number. Consequently, equation (2.5) implies that  $\xi^2 \Phi(\xi)$  increases at the high- $\xi$  region as  $R_\lambda$  decreases. It should be emphasized that this Reynolds-number dependence only applies to flows at low Reynolds numbers where the energy-containing scales contributing significantly to the integral (2.6) are not well separated from the dissipative scales contributing significantly to the integral (2.5). At high Reynolds number, almost all the contribution to the integral (2.6) is from the region  $\xi \ll 1$  only; thus, the Reynolds-number dependence implied by (2.6) is not noticeable on a plot of  $\xi^2 \Phi(\xi)$  against  $\xi$ .

Similar Reynolds-number dependence is also found for the normalized one-dimensional spectrum  $(k_1 \eta)^2 \Phi_{11}(k_1 \eta)$ , with  $\Phi_{11}(k_1 \eta) \equiv E_{11}(k_1) / (\bar{\epsilon} v^5)^{1/4}$ . For  $R_\lambda > 100$ , the second moment  $(k_1 \eta)^2 \Phi_{11}(k_1 \eta)$  has a peak value of 0.25 at  $k_1 \eta = 0.8$ , in very good agreement with the experimental data obtained by Champagne (1978) for a cylinder wake flow at  $R_\lambda = 138$ . However, the Reynolds-number dependence shown here for very low Reynolds numbers is in contrast with the results of Champagne (1978) for relatively higher Reynolds numbers, i.e.  $R_\lambda \sim 138$  to 7000, which show that the tail of the fourth moment  $(k_1 \eta)^4 \Phi_{11}(k_1 \eta)$  increases with increasing Reynolds-number. Champagne (1978), following Wyngaard & Tennekes (1970), relates this different Reynolds-number dependence to the monotonic increase of velocity-derivative skewness with Reynolds number observed in their measurements. However, the velocity-derivative skewness in our simulations shows almost no Reynolds number dependence. Therefore, our observation of spectrum collapse for  $R_\lambda > 100$  does not contradict with the argument of Champagne (1978) and Wyngaard & Tennekes (1970). In view of the

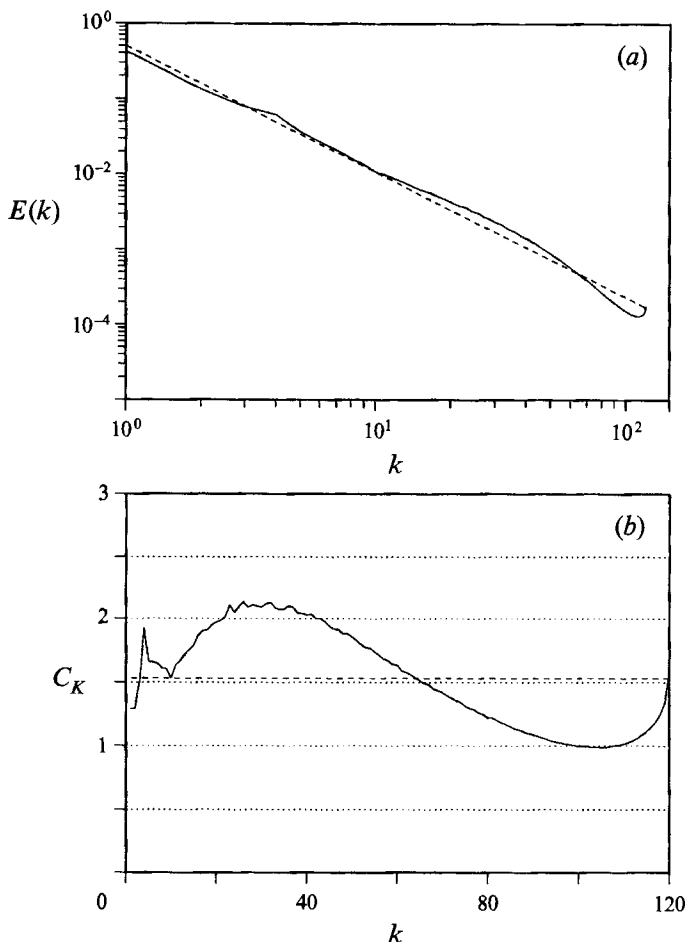


FIGURE 3. (a) The three-dimensional energy spectrum and (b) the local Kolmogorov constant  $C_K \equiv E(k)k^{5/3}/\bar{\epsilon}^{2/3}$  as a function of the wavenumber  $k$  for the large-eddy simulation flow field. The dashed line in (a) marks the  $-5/3$  slope. The dashed line in (b) marks the mean value of  $C_K$  ( $C_K = 1.532$ ).

experimental difficulties in constructing true isotropic flow fields and in measuring high-wavenumber spectra and high-order moments of velocity derivatives (Champagne 1978), the question of whether a Reynolds-number dependence of the energy spectrum for isotropic turbulence exists at very high Reynolds numbers requires further investigation.

To confirm the isotropy of the simulated flows, we computed an isotropy coefficient, defined as

$$\frac{E_{11}(k_1) - k_1 \partial E_{11}(k_1) / \partial k_1}{E_{22}(k_1) + E_{33}(k_1)}, \quad (2.7)$$

where  $E_{22}$  and  $E_{33}$  are transverse one-dimensional spectra (Champagne 1978). This quantity should be equal to 1.0 for an isotropic field. We find that the isotropy coefficient fluctuates around 1 with less than 10% deviations for  $k_1 \eta > 0.1$  in all fields. Departures from 1 at lower  $k_1 \eta$  are due to fewer samples at the largest scales. Similar behaviour was observed by Jiménez *et al.* (1993).

The energy spectrum for the LES field is shown in figure 3. The spectrum oscillates

around a  $k^{-5/3}$  slope, as shown more clearly in figure 3 where the *local* Kolmogorov coefficient, defined as  $C_K(k) = E(k)k^{5/3}/\bar{\epsilon}^{2/3}$ , is plotted against  $k$  on a linear-linear plot. The mean dissipation  $\bar{\epsilon}$  is again estimated as the energy flux from the resolved field to the subgrid scales.  $C_K(k)$  varies in the range from 1.0 to 2.2, with an average value of 1.532.

Table 1 also shows estimated physical-space length scales corresponding to the wavenumber of the peak dissipation  $k_D = \pi/r_D$ , the peak energy  $k_E = \pi/r_E$ , and the minimum non-forced wavenumber  $k_F = \pi/r_F$ . The relation  $r = \pi/k$  follows from relating the minimum length scale on the grid,  $2\pi/N$ , to the maximum computed wavenumber,  $N/2$ . These length scales, to be used later, should only be taken as estimates owing to the arbitrariness in relating physical- and Fourier-space scales and to the possible oscillations in the spectra. Note that the scale separation as defined by  $r_E/r_D$  is about 21 for the forced  $512^3$  forced DNS field.

Recently, Tsinober *et al.* (1992) used a twelve-wire hot-wire probe to measure all nine velocity gradients in approximately isotropic grid turbulence at  $R_\lambda \approx 72$  and presented detailed direct experimental quantification of fine-scale statistics. Their experimental results are compared with our simulations in the four quantities, at the end of table 1. The first three are the normalized r.m.s., skewness, and flatness of the dissipation fluctuations  $\zeta \equiv \epsilon - \bar{\epsilon}$ . The last parameter is the normalized enstrophy production  $\overline{\omega_i \omega_j s_{ij}} / (\overline{\omega^2 s_{ij} s_{ij}})^{1/2}$ . The dissipation ‘intermittency parameter’  $(\overline{\zeta^2})^{1/2}/\bar{\epsilon}$  increases slowly with  $R_\lambda$  for  $R_\lambda > 100$  in our simulations, with the experimental value lying within these values. The skewness and flatness of the dissipation-rate fluctuations increase much more rapidly with Reynolds number, and are much larger than the experimental value. Since both  $S_\zeta$  and  $F_\zeta$  are strongly influenced by dissipation-range scales, they are probably underestimated in the experiment owing to the finite probe resolution and other difficulties as noted in Tsinober *et al.* (1992).

Particularly interesting is the result that the normalized enstrophy production is nearly independent of  $R_\lambda$ , with an average value of  $0.22 \pm 0.1$ . Again the experimental value is likely to be an underestimate. The simulations suggest that the value of the normalized enstrophy production may be *universal* at higher Reynolds number with a value of about 0.22, providing a useful parameter for turbulence modelling. In isotropic turbulence, the normalized enstrophy production is directly related to the longitudinal velocity derivative skewness

$$\frac{\overline{\omega_i \omega_j s_{ij}}}{\overline{\omega^2 (s_{ij} s_{ij})}^{1/2}} = -\frac{7}{3} \frac{1}{\sqrt{30}} S = -0.426S, \quad (2.8)$$

which follows from the relation (Champagne 1978)

$$\overline{\omega_i \omega_j \frac{\partial u_i}{\partial x_j}} = -\frac{35}{2} \overline{\left(\frac{\partial u_1}{\partial x_1}\right)^3} \quad (2.9)$$

in isotropic turbulence. Potential universality in normalized enstrophy production is therefore directly related to potential universality in skewness. A value of  $S = -0.50$  gives the normalized enstrophy production of 0.21, in good agreement with the directly computed values.

The structure of the enstrophy field is shown with enstrophy isosurfaces in figure 4 in subdomains which are two integral length scales on a side. In the two DNS fields with  $R_\lambda$  of 21 and 195 (figures 4a and 4b), the regions of high vorticity appear as tubes, especially in the higher Reynolds number simulation. The tube-like structures become more elongated as Reynolds number increases, in agreement with the results

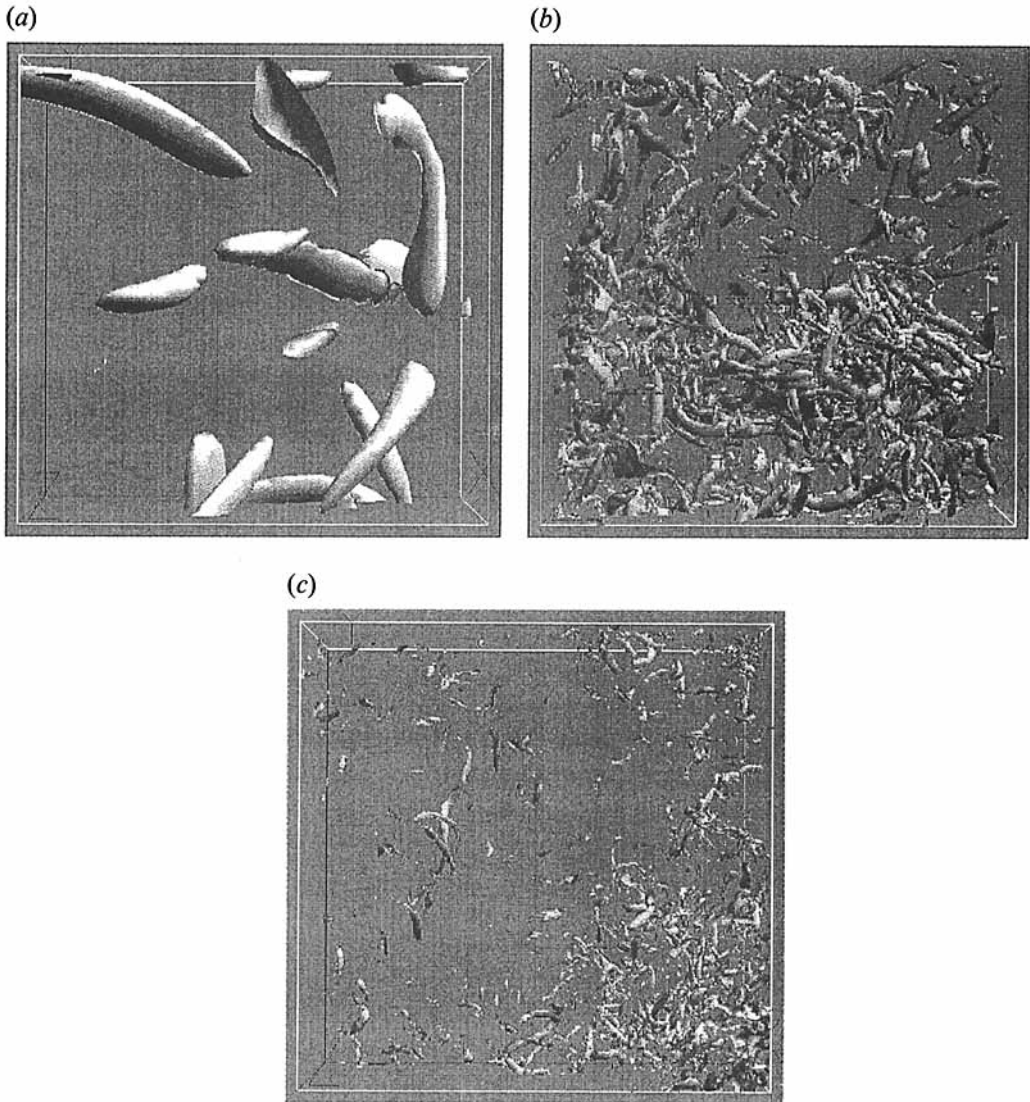


FIGURE 4. Isosurface of vorticity magnitude in a subdomain of side  $2L_f$  for three different flow fields. (a) d256c2,  $Re_\lambda = 68$ , threshold  $|\omega| = 4\omega'$ , about 2% volume covered; (b) f512,  $Re_\lambda = 195$ , threshold  $|\omega| = 4\omega'$ , about 3% volume covered; (c) large-eddy simulation les256, threshold is chosen such that about 1.5% volume is covered.  $\omega' \equiv [(\omega \cdot \omega)/3]^{1/2}$  is the r.m.s. component vorticity fluctuation.

of Jiménez *et al.* (1993). A quantitative analysis shows that the high-ensrophy regions contain a higher percentage of total integrated enstrophy as  $R_\lambda$  increases if the volume covered by the these regions is held fixed, indicating that the vorticity field becomes more intermittent as  $R_\lambda$  increases.

Although the LES removes most of the vorticity from an equivalent fully resolved simulation, it is interesting that tube-like structures still persist in the weakly resolved vorticity field, as shown visually in figure 4(c). Here the threshold was chosen such that the isosurfaces cover about 1.5% of the total volume. These high-intensity regions of the filtered vorticity appear as very thin, non-uniformly distributed tubes, with tube

size on the order of grid spacing. Figure 4(c) shows more clearly the existence of tube-like structures in LES than the visualization of Métais & Lesieur (1992) for a similar  $96^3$  LES.

The comparisons we have made in this section suggest that the higher Reynolds number forced direct numerical simulations have realistic flow features for both the dissipation and inertial subrange scales that are representative of high Reynolds number isotropic turbulence. The LES field, while not representing the fine scales below the grid spacing, provides a more extended inertial subrange than DNS with realistic structure in the resolved scales.

### 3. Probability distribution of dissipation fluctuations

#### 3.1. Methodology

We focus in this section on the first aspect of the K62 theory as discussed in §1, the form of the probability distribution of the locally volume-averaged dissipation fluctuations  $\epsilon_r$ . In general, the p.d.f. is function of both the flow Reynolds number  $R_\lambda$  and the local scale  $r$ .

We analyse primarily fields d256c1 for freely decaying turbulence at  $R_\lambda = 68$ , f256 for forced turbulence at  $R_\lambda = 151$ , and the LES given by les256 (see table 1). Because these flows are closely isotropic, we calculate velocity increments in the  $x$ -direction only,  $\Delta_r u(x, y, z, t) \equiv u(x + \frac{1}{2}r, y, z, t) - u(x - \frac{1}{2}r, y, z, t)$ . The local dissipation rate  $\epsilon$  is computed in physical space from  $\epsilon = 2\nu s_{ij}s_{ij}$ . Because  $\epsilon$  is defined on the grid, we use multiples of the grid spacing  $\Delta$  as the averaging scale  $r$ , so that

$$\epsilon_r(x) = \frac{1}{m} \sum_{i=-(m-1)/2}^{i=+(m-1)/2} \epsilon(x + i\Delta) \quad \text{for } r = m\Delta, \quad m = 3, 5, 7, \dots, \quad (3.1a)$$

$$\epsilon_r(x) = \frac{1}{m} \sum_{i=1-m/2}^{i=m/2} \epsilon(x + i\Delta) \quad \text{for } r = m\Delta, \quad m = 2, 4, 6, \dots, \quad (3.1b)$$

where the dependence on  $y, z, t$  is not shown and  $x$  is located at a grid point. At the minimum value for  $r$  ( $r = \Delta$ ) we take  $\epsilon_r(x) = \epsilon(x)$ . Equation (3.1) defines a line averaging rather than a spherical-volume-averaging. We use line averaging throughout the paper as it is simpler to compute and more consistent with the way that the velocity increment is calculated. Test runs using cubic-volume averaged  $\epsilon_r$  show qualitatively the same results as will be discussed here.

The corresponding velocity increments are then given by

$$\delta_r u(x) = \left| u(x + \frac{m}{2}\Delta) - u(x - \frac{m}{2}\Delta) \right| \quad \text{for } r = m\Delta, \quad m = 1, 3, 5, 7, \dots, \quad (3.2a)$$

$$\delta_r u(x) = \left| u(x + \frac{m+1}{2}\Delta) - u(x - \frac{m-1}{2}\Delta) \right| \quad \text{for } r = m\Delta, \quad m = 2, 4, 6, \dots, \quad (3.2b)$$

where the velocity grid is shifted by  $\Delta/2$  in the  $x$ -direction for the computation of  $\Delta_r u(x)$ . The shifting is carried out in Fourier space by multiplying the Fourier coefficients by a factor of  $\exp(ik_1\Delta/2)$  before transforming the velocity field back to the physical space.



The above averaging is equivalent to a discretized version of the following one-dimensional box-filter averaging:

$$\epsilon_r(x) = \frac{1}{r} \int_{-r/2}^{r/2} \epsilon(x+h) dh, \quad (3.3)$$

which can be carried out by filtering  $\epsilon(x)$  in Fourier space as

$$\hat{\epsilon}_r(k_1) = \hat{\epsilon}(k_1) \frac{\sin \frac{1}{2}rk_1}{\frac{1}{2}rk_1}, \quad (3.4)$$

where  $\hat{\epsilon}_r(k_1)$  and  $\hat{\epsilon}(k_1)$  are Fourier coefficients of  $\epsilon_r$  and  $\epsilon$ , respectively. Spatial averaging smooths spiky structures in the signal, reducing the level of dissipation fluctuations. Equation (3.4) shows that the averaging removes high-wavenumber contributions to the *variance* of the dissipation fluctuations at a rate proportional to  $k_1^{-2}$ . The box filter is often used in LES to define a resolved turbulent field (e.g. Piomelli *et al.* 1991). This alternative approach was also tested and was found to give nearly the same result as equation (3.1), but with the disadvantage that, when transforming back to the physical space, the positive-definite property of  $\epsilon_r$  is not guaranteed due to the small aliasing error. Because  $\epsilon_r$  was found to be negative at a few grid points, this alternative approach was not used.

In addition to the fully resolved direct simulations, we found it useful to apply the large-eddy simulation data to the analysis of the K62 theory in the inertial range. However, the dissipation-rate spectrum is not resolved in LES with a filter cut-off in the inertial range. We approximate volume-averaged dissipation  $\epsilon_r$  with the volume-averaged energy flux from the resolved scales to the unresolved scales using an eddy-viscosity-based subgrid-scale model. This energy flux is converted to the viscous dissipation in the unresolved scales. Using the eddy viscosity model, the flux at the filter scale  $\Delta$  is given by

$$F^\Delta = 2\nu_t \tilde{s}_{ij} \tilde{s}_{ij}, \quad (3.5)$$

where  $\tilde{s}_{ij}$  is the strain-rate tensor computed from the resolved velocity field  $\tilde{u}_i(\mathbf{x})$ . Métais & Lesieur (1992) have shown that  $F^\Delta$  well approximates the local energy flux from resolved to subgrid scales in homogeneous turbulence when the eddy viscosity is independent of position.

In equilibrium turbulence, the energy flux into the subgrid volume  $\Delta^3$  is dissipated within that volume on average. Consequently  $F^\Delta$  is a good approximation for the average dissipation rate in the subgrid-scale volume and we may write

$$\epsilon_{r=\Delta}(\mathbf{x}) \approx F^\Delta(\mathbf{x}). \quad (3.6)$$

Similar approaches have been used by Peltier & Wyngaard (1995) to approximate dissipation rates in a convective boundary layer obtained from LES. The eddy viscosity  $\nu_t$  is very close to a constant for  $k/k_c < 0.3$ , and is approximately equal to (Kraichnan 1976; Métais & Lesieur 1992),

$$\nu_t \approx 0.267 C_k^{1/2} \bar{\epsilon}^{1/3} k_c^{-4/3}, \quad (3.7)$$

where  $k_c$  is the filter cutoff wavenumber. Because  $\epsilon_r = (\epsilon_\Delta)_r$  when  $r \gg \Delta$ ,  $\epsilon_r$  for  $r \gg \Delta$  may be approximated by averaging  $F^\Delta$  over  $r$ . We apply this approximation for  $r \geq 10\Delta$ .

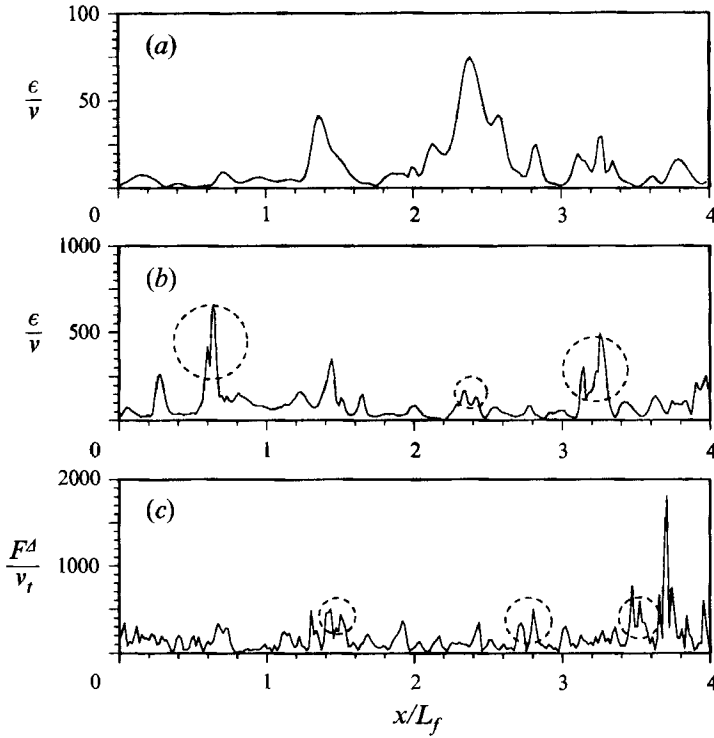


FIGURE 5. The local dissipation rate or energy flux (for the LES field only) on a line  $y = z = L_B/2$  of length 4 integral length scales in the simulation box. (a) d256c2,  $Re_\lambda = 68$ ; (b) f256,  $Re_\lambda = 151$ ; and (c) les256. The circles mark the events with two peaks occurring adjacent to one another.

### 3.2. Distribution of volume-averaged dissipation fluctuations

Figure 5 shows the local dissipation rate on a line of length  $4L_f$  for three representative fields at different  $R_\lambda$ , where  $F^\Delta$  in figure 5(c) can be viewed as local dissipation at a much higher *effective* Reynolds number averaged over grid scale  $\Delta$ . Visually, the local dissipation becomes more spiky as  $R_\lambda$  increases, and the number of spikes in one integral length scale grows with  $R_\lambda$ . We often observe two dissipation peaks adjacent to one another, possibly a reflection of the local dissipation-rate field surrounding vortex tubes (see figure 4).

Figure 6 gives the probability distribution of  $\ln \epsilon_r$  at four different  $r$  for forced turbulence at  $R_\lambda = 151$ . Here  $\ln \epsilon_r$  is centred on its mean  $m_r \equiv \overline{\ln \epsilon_r}$  and normalized by its standard deviation  $\sigma_r \equiv [(\overline{\ln \epsilon_r - m_r})^2]^{1/2}$ . For convenience, we define  $s_r \equiv (\ln \epsilon_r - m_r)/\sigma_r$ . Also shown is the standard Gaussian distribution for comparison. Figure 6 shows that whereas  $\ln \epsilon_r$  is nearly Gaussian for  $|s_r| \leq 2$ , the tails deviate significantly from the Gaussian distribution. Furthermore,  $\ln \epsilon_r$  is negatively skewed at all  $r$ , consistent with the findings of Vincent & Meneguzzi (1991) who showed similar p.d.f.s for  $\ln \epsilon$ . However, we find that these deviations from Gaussianity are greatest at small  $r$ , and appear to reduce as  $r$  increases. The probability distributions of  $\ln \epsilon_r$  for other DNS fields and the LES field are similar. We find that the skewness of  $\ln \epsilon_r$  lies in the range  $-0.15$  to  $-0.20$  for small  $r$  and approaches zero as  $r \rightarrow L_f$ , while the flatness of  $\ln \epsilon_r$  is in the range 2.9 to 3.2, close to 3 for the Gaussian distribution.

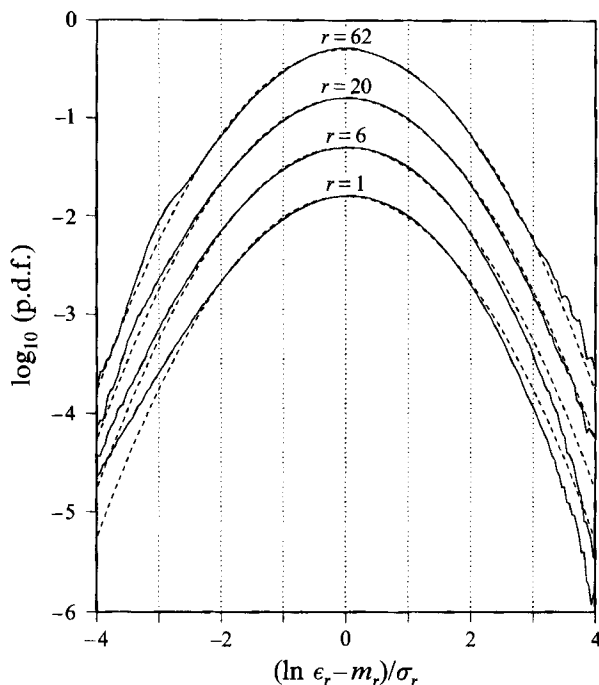


FIGURE 6. Probability density function for the log-dissipation,  $\ln \epsilon_r$ , at four different  $r$  of 1, 6, 20, 62 grid spacings for the forced DNS field at  $Re_\lambda = 151$ . The curves are shifted by different amounts for  $r > 1$ . The dash lines represent the normal distribution.

More detailed comparisons with the log-normal distribution can be made by computing moments of volume-averaged dissipation rate,  $\overline{\epsilon_r^n}$ . For a log-normal distribution (Kolmogorov 1962),

$$\overline{\epsilon_r^n} = \exp(nm_r + \frac{1}{2}n^2\sigma_r^2). \quad (3.8)$$

Using  $\overline{\epsilon_r} = \bar{\epsilon}$  yields for  $n = 1$ ,

$$Q \equiv \frac{m_r + \frac{1}{2}\sigma_r^2}{\ln \bar{\epsilon}} = 1, \quad (3.9)$$

implying that the mean and standard deviation of  $\ln \epsilon_r$  are directly related if the distribution of  $\epsilon_r$  is log-normal. Figure 7 shows  $Q$  as a function of  $r$  for the three fields used in figure 5. Overall,  $Q$  is within 1% of deviations from log-normality at all  $r$ , and improves with increasing  $r$ , suggesting that the log-normal model is accurate for the first-order moment  $n = 1$ . However, the departures from the log-normal distribution apparent in figure 6 become more important in higher-order moments. To see this, we plot the non-dimensional ratio

$$R_n \equiv \frac{2}{n(n-1)} \times \frac{\ln \overline{\epsilon_r^n}/(\bar{\epsilon})^n}{\ln \overline{\epsilon_r^2}/(\bar{\epsilon})^2}, \quad (3.10)$$

against  $n$  in figure 8 for fixed  $r$ , where  $R_n = 1$  when  $n > 2$  if  $\epsilon_r$  is precisely log-normal. Note that  $R_2$  is defined to be 1. Overall,  $R_n$  decreases continuously with increasing  $n$ , indicating that the log-normal model tends to overpredict the magnitude of high-order moments. The departure from log-normality decreases as  $r$  increases and approaches

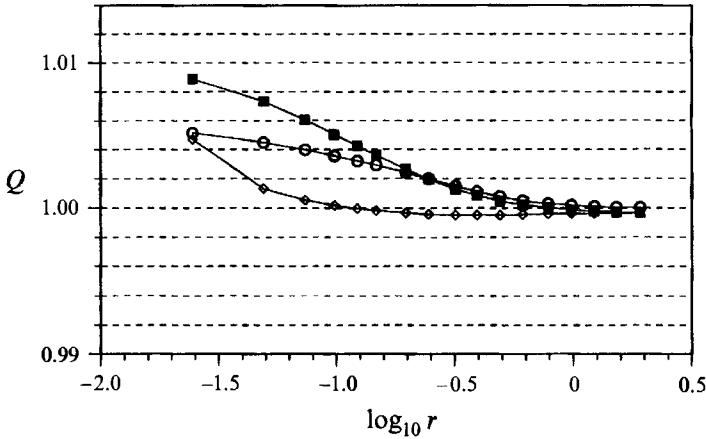


FIGURE 7. The ratio  $Q \equiv (m_r + 0.5\sigma_r^2)/\ln \bar{\epsilon}$  for the three different types of flow fields. ■,  $256^3$ , free-decaying flow at  $Re_\lambda = 68.1$ ; ○,  $256^3$ , forced stationary flow at  $Re_\lambda = 151$ ; ◇,  $256^3$ , large-eddy simulation.

inertial-range scales. Furthermore, the departure is less for higher flow Reynolds number  $R_\lambda$ . We also studied the p.d.f. of the ratio  $\epsilon_{r_2}/\epsilon_{r_1}$  ( $r_1 > r_2$ ) and found that it is closer to a log-Poisson distribution in the narrow inertial subrange as suggested by She & Waymire (1995), than to a log-normal distribution, but the p.d.f. of  $\epsilon_r$  is better approximated by a log-normal distribution. A detailed comparison of the log-normal model with the log-Poisson model will be presented in a future publication.

The dependence of the variance of  $\ln \epsilon_r$  on  $r$  is shown in figure 9 on a linear-log plot to determine the value of  $\mu$  in equation (1.6). Whereas the LES field does not display a well-defined linear region, it appears to have an average slope of approximately  $\mu = 0.2$ , very close to the measured value by Anselmet *et al.* (1984), Sreenivasan & Kailasnath (1993), and Praskovsky & Oncley (1994). The DNS fields, on the other hand, display short linear regions at intermediate  $r$  with an approximate slope  $\mu = 0.28$ . This  $\mu$  value is only an estimate, which is the best one can offer at the moment.

In summary, whereas the probability distribution of  $\epsilon_r$  is close to log-normal at small-to-moderate fluctuation levels and at large  $r$ , significant departures from the log-normal distribution exist in the tails which increase with decreasing  $r$ . These departures cause an overprediction of the higher-order moments of dissipation-rate fluctuations. Although the degree of departure appears to decrease as  $r$  moves into the inertial subrange and as flow Reynolds number  $R_\lambda$  increases, the departures of high-order ( $n \geq 5$ ) moments from log-normality is significant even for the inertial subrange.

#### 4. Direct examination of the refined similarity hypotheses

We are now in a position to analyse directly the K62 refined similarity hypotheses, specifically the relationship between the conditionally averaged velocity increment  $\overline{\delta_r u | \epsilon_r}$  and the locally averaged dissipation rate  $\epsilon_r$ . To compute the averaged velocity increments,  $\overline{\delta_r u | \epsilon_r}$ , the following procedure was used: (i) divide the dissipation value  $\epsilon_r$  into bins of small width and (ii) for each  $\epsilon_r$  bin, compute the average velocity increment  $\overline{\delta_r u | \epsilon_r}$  based on those spatial points where the  $\epsilon_r$  value is located in the

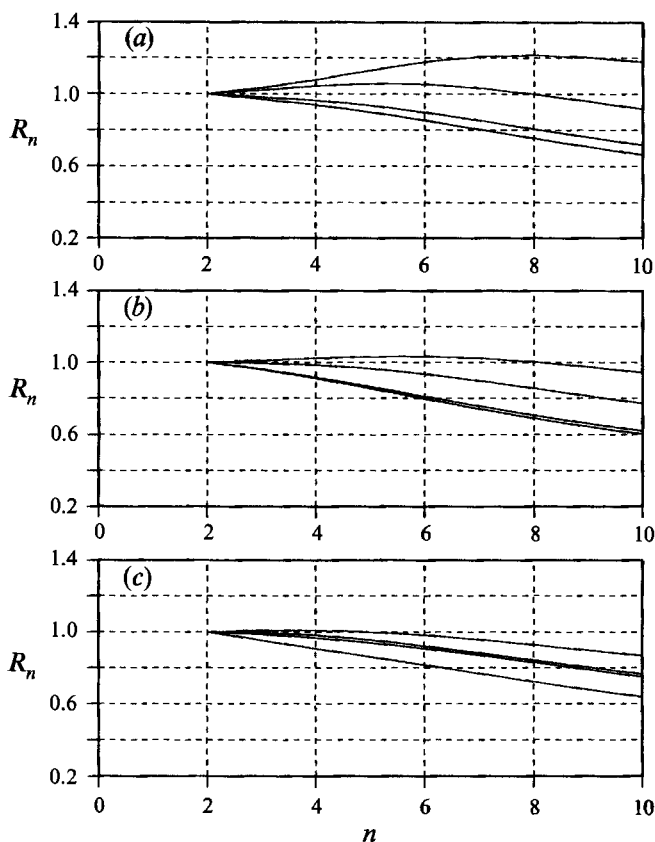


FIGURE 8. The nondimensional ratio defined by equation (3.10) for the three different flow fields. The four lines in each plot, from bottom to top, are for  $r = \Delta, 6\Delta, 20\Delta, 62\Delta$ , respectively. (a) d256c2,  $Re_\lambda = 68$ ; (b) f256,  $Re_\lambda = 151$ ; and (c) les256.

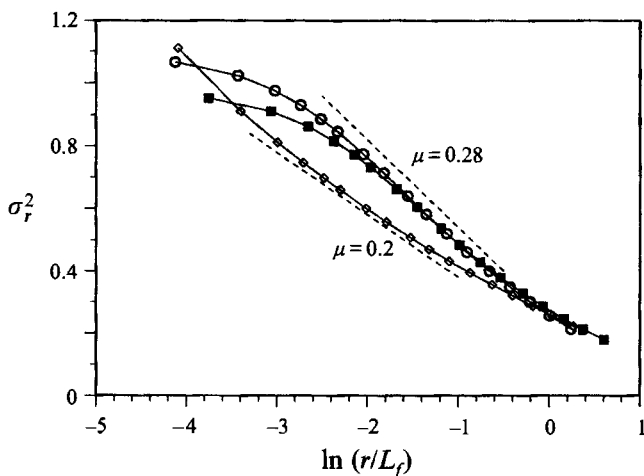


FIGURE 9. The scaling for the variance of  $\ln \epsilon_r$ . ■,  $256^3$ , free-decaying flow at  $Re_\lambda = 68.1$ ; ○,  $256^3$ , forced stationary flow at  $Re_\lambda = 151$ ; ◇,  $256^3$ , large-eddy simulation.

bin. Whereas Chen *et al.* (1993) used linear bins in  $\epsilon_r$ , here we divide  $\ln \epsilon_r$  into bins of uniform width. We use logarithmic bins because  $\epsilon_r$  is approximately log-normally distributed (§3), thus distributing the samples more uniformly among different bins. As importantly, because the power-law scaling exponents are extracted from log-log plots of  $\overline{\delta_r u | \epsilon_r}$  against  $\epsilon_r$ , the use of logarithmic bins extends the range of  $\ln \epsilon_r$  on the log-log plots and allows more accurate determination of the scaling exponents. In this study, we divide the normalized, logarithmic dissipation rate  $s_r \equiv (\ln \epsilon_r - \overline{\ln \epsilon_r}) / \sigma_r$  into 201 equally spaced bins from  $s_r = -4$  to  $+4$ , and compute  $\overline{\delta_r u | \epsilon_r}$  for each bin, for each fixed  $r$ . The computation was repeated over roughly logarithmically distributed values of  $r$ , with  $r_{i+1} \approx 1.25r_i$ .

#### 4.1. Scaling exponent of $\epsilon_r$

We first examine the scaling exponent of  $\epsilon_r$  for the conditionally averaged velocity increments. For this purpose, log-log plots of  $\overline{\delta_r u | \epsilon_r}$  against  $\epsilon_r$  are presented. In figure 10(a) we plot  $\ln(\overline{\delta_r u | \epsilon_r}) / \sigma_r$  against  $s_r$  on a log-log scale for the forced DNS field at  $R_\lambda = 151$ . This normalization places the curves at different fixed  $r$  in a similar range along the abscissa. Only the bins with at least 1000 samples are plotted; 17 curves with different  $r$  are shown, where  $r$  varies from  $r_1 = \Delta \approx 1.7\eta$  (bottom curve) to  $r_{17} = 78\Delta \approx 1.3L_f$  (top).

The first observation to be made from figure 10(a) is that  $\overline{\delta_r u | \epsilon_r}$  increases with  $\epsilon_r$  and thus is *positively* correlated with  $\epsilon_r$  at all  $r$ . For small-to-intermediate values of  $r$ , the dependence is linear on this log-log plot, which implies

$$\overline{\delta_r u | \epsilon_r} \propto \epsilon_r^\alpha. \quad (4.1)$$

For small  $r$ , the slope is very close to  $1/2$  for the whole range of  $\epsilon_r$ , which is expected based on a Taylor series expansion around  $r = 0$ . As  $r$  increases, the range of the straight-line segment and its slope gradually decrease. The slope approaches the value of  $1/3$ , the inertial-range value given by the second RSH, equation (1.9), in the range  $-3 \lesssim s_r \lesssim -1$  for  $r \sim 0.4L_f - 0.8L_f$ . At these larger values of  $r$  the slope seems to change when  $s_r \gtrsim -1$ , indicating that the RSH prediction may be more accurate in the low-magnitude fluctuations of  $\epsilon_r$  (those below the mean). These observations are consistent with the recent work by Chen *et al.* (1993).

In order to quantify the slopes of the curves in figure 10(a), curve segments were least-squared fit with a straight line. Figure 10(b) shows the scaling exponent obtained in this way as a function of  $r$  for the three different portions of the curves shown in figure 10(a):  $-3 \leq s_r < -1$  (dashed),  $-1 \leq s_r < 1$  (solid), and  $1 \leq s_r < 3$  (dotted). In general the scaling exponent decreases with increasing  $r$ . For  $s_r < 1$ , the scaling exponent is very close to  $0.5$  for  $\log_{10} r < -1.0$  ( $r/\eta < 7$ ) so the far-dissipation-range scaling is reached at a scale greater than the Kolmogorov scale. The scaling exponent for  $-3 < s_r < -1$  has a value very close to  $1/3$  as  $r \rightarrow L_f$ , in quantitative agreement with the second RSH.† We stress that only the direction of the scaling exponent variation seems to conform with K62 hypotheses. An extended  $\alpha = 1/3$  range is not reached here due to a very limited scale separation. In the range  $1 < s_r < 3$ , the

† In a natural turbulence, the RSH does not apply as  $r \rightarrow L_f$ . In this numerical turbulence the lowest modes are forced to follow a  $k^{-5/3}$  energy spectrum, which might extend the applicability of RSH to  $r$  closer to  $L_f$ . Viewing it alternatively, the inertial-range fluid motions are shifted to an energy-containing range of scales, and thus effectively the computed  $L_f$  in the simulation is an underestimate compared to natural turbulence.

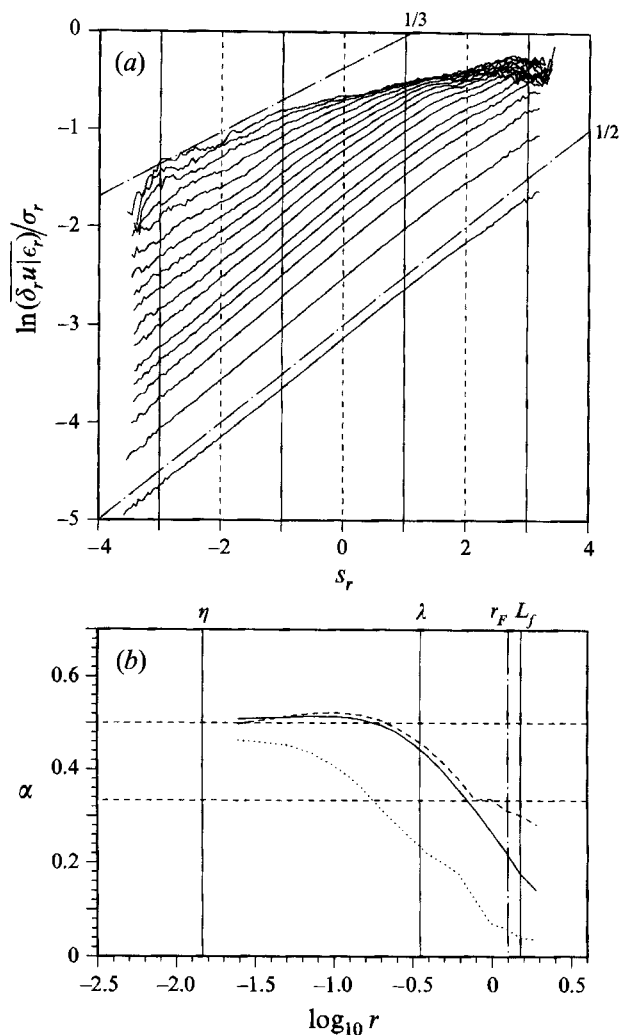


FIGURE 10. (a) Velocity increment conditioned on the locally averaged dissipation,  $\delta_r u | \epsilon_r$ , against  $\epsilon_r$  on a log-log plot, for the  $256^3$  forced DNS field f256 at  $Re_\lambda = 151$ . Each curve corresponds to a fixed  $r$ , where from bottom to top,  $r$  varies from  $r_1 = \Delta = 1.7\eta$  to  $r_{17} = 78\Delta = 1.3L_f$  such that  $r_{i+1} \approx 1.25r_i$ . The upper and lower chained-dotted lines show slopes  $\alpha$  of  $\frac{1}{2}$  and  $\frac{1}{3}$ , respectively, where  $\overline{\delta u | \epsilon_r} \propto \epsilon_r^\alpha$ . (b) The power-law exponent  $\alpha$  obtained as the average slope in (a) for the three regions  $-3 \leq s_r < -1$  (dashed line),  $-1 \leq s_r < 1$  (solid line), and  $1 \leq s_r < 3$  (dotted line) as a function of  $r$ . Two horizontal lines mark the levels of  $\frac{1}{2}$  and  $\frac{1}{3}$ , and the vertical lines mark the various characteristic length scales in the flow field.

scaling exponent approaches zero as  $r \rightarrow L_f$ . In principle, the scaling exponent should go to zero if  $r \gg L_f$ .

The results for the  $512^3$  forced DNS field (f512) at  $R_\lambda = 195$  are shown in figure 11. 20 different  $r$  values were used, with  $r_1 = \Delta \approx 1.5\eta$  and  $r_{20} = 152\Delta \approx 1.3L_f$ . Only the bins with at least 8000 samples are shown in figure 11(a). Because the number of samples per bin is about 8 times larger in figure 11 than in figure 10, the curves in figure 11(a) are somewhat smoother for large  $r$ . However, the number of independent samples may not be much different for large  $r$ . Again for small-to-intermediate  $r$

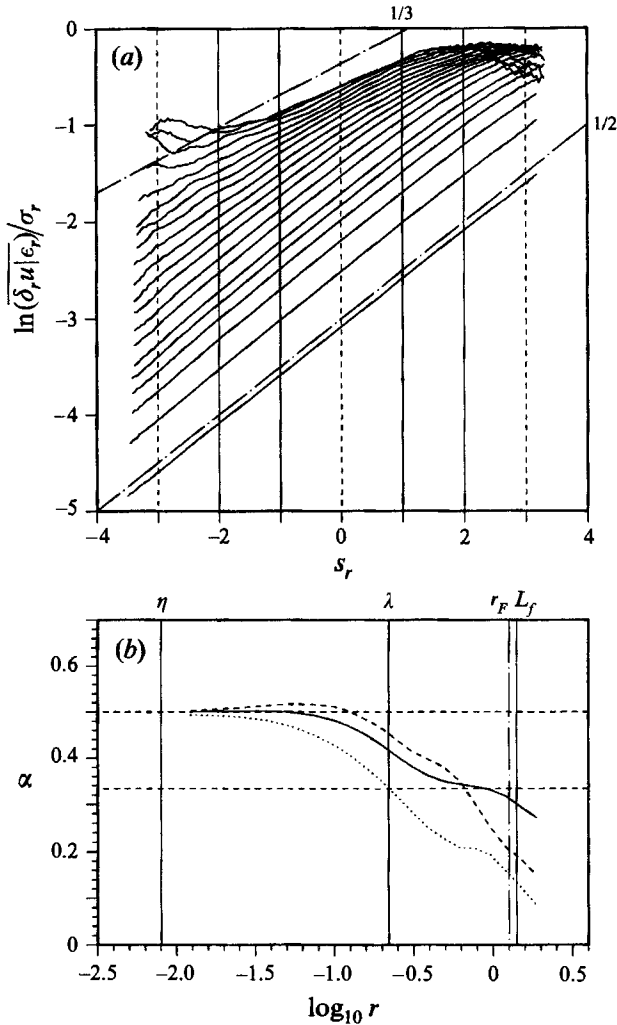


FIGURE 11. (a) Velocity increment conditioned on the locally averaged dissipation,  $\overline{\delta_r u | \epsilon_r}$ , against  $\epsilon_r$  on a log-log plot, for the  $512^3$  forced DNS field at  $Re_\lambda = 195$ . Each curve corresponds to a fixed  $r$ , and from bottom to top,  $r$  changes from  $r_1 = \Delta = 1.5\eta$  to  $r_{20} = 152\Delta = 1.3L_f$ . (b) The power-law exponent  $\alpha$  obtained as the average slope in (a) for the three regions  $-2 \leq s_r < -1$  (dashed line),  $-1 \leq s_r < 1$  (solid line), and  $1 \leq s_r < 2$  (dotted line) as a function of  $r$ .

values, the dependence of  $\overline{\delta_r u | \epsilon_r}$  on  $\epsilon_r$  is well defined by a power law. The average scaling exponents for the three regions,  $-2 < s_r < -1$ ,  $-1 < s_r < 1$ , and  $1 < s_r < 2$  are shown in figure 11(b). The scaling exponent for the central region,  $-1 < s_r < 1$ , which accounts for about 70% of data set, exhibits a weak plateau near  $\alpha = 1/3$  between  $r = \lambda$  and  $r = L_f$ . Although the inertial subrange in the flow is not very wide in this simulation, the results suggest that a more extended  $\alpha = 1/3$  range may exist with an extended inertial range at higher Reynolds numbers.

The scaling exponents for the other two  $s_r$  ranges in figure 11(b) indicate a weak plateau in the region  $\lambda < r < L_f$ , but with levels different from  $1/3$ . In all ranges of  $s_r$ , the scaling exponents rapidly decrease as  $r$  increases beyond the integral scale  $L_f$ . On the other hand, as  $r \rightarrow \eta$  the scaling exponents all approach 0.5, even more



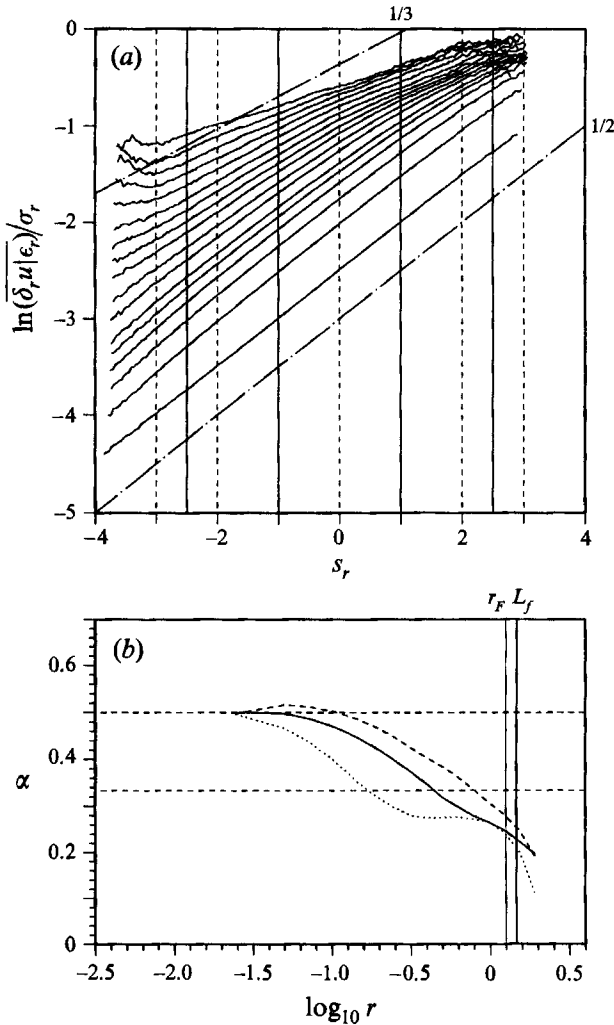


FIGURE 12. (a) Velocity increment conditioned on the locally averaged dissipation,  $\overline{\delta_r u | \epsilon_r}$ , against  $\epsilon_r$  on a log-log plot, for the  $256^3$  large-eddy simulation field. Each curve corresponds to a fixed  $r$ , and from bottom to top,  $r$  changes from  $r_1 = \Delta$  to  $r_{17} = 78\Delta = 1.3L_f$ . (b) The power-law exponent  $\alpha$  obtained as the average slope in (a) for the three regions  $-2.5 \leq s_r < -1$  (dashed line),  $-1 \leq s_r < 1$  (solid line), and  $1 \leq s_r < 2.5$  (dotted line) as a function of  $r$ .

consistently than in figure 10. Similar results were found for the  $128^3$  forced DNS field, except there is no plateau region of  $\alpha \sim 1/3$  at all due to the low Reynolds numbers.

Figure 12 shows similar results for the  $256^3$  LES field, where  $\epsilon_r$  is approximated using the flux to the subgrid scales, as described in §3. Interestingly, the scaling exponent is equal to 0.5 at  $r = \Delta$ , indicating that the resolved field is sufficiently smooth at this scale for a Taylor series expansion to apply. Again we observe a positive correlation between the conditionally averaged velocity increment and the locally averaged dissipation rate. We also observe power-law dependence between  $\overline{\delta_r u | \epsilon_r}$  and  $\epsilon_r$  at all  $r$  over broad  $s_r$  regions. Even though a more extended inertial subrange is produced by LES, a more extended  $\alpha = 1/3$  plateau (compared to the

512<sup>3</sup> DNS field shown in figure 11, for example) is not observed. (The plateau for  $1 < s_r < 2.5$  at  $\alpha = 0.26$  represents a small part of the flow and is significantly below 1/3.) This lack of a well-defined plateau may be a consequence of approximating the locally averaged dissipation with the modelled energy flux from the resolved velocity field. A different approach will be discussed in §4.3 which reveals a ‘hidden’ inertial subrange in the context of the second RSH.

Some general observations can be made from figures 10 to 12, relevant to all flow types. (Similar results for the decaying flows exist, although not shown here.) For a given  $r$ , the scaling exponent  $\alpha$  tends to be largest for the smallest  $s_r$  (or  $\epsilon_r$ ), and decreases with increasing  $s_r$  (or  $\epsilon_r$ ). Since  $Re_{\epsilon_r} = \epsilon_r^{1/3} r^{4/3} / \nu$ , we might expect  $\alpha$  plotted against  $r$  to cross 1/3 at larger  $\epsilon_r$  before smaller  $\epsilon_r$ . Figures 10 to 12 indicate that this is the case (compare the dotted line with the dashed line in  $\alpha$  versus  $r$  plots). With the same reasoning, one may also expect a more extended  $\alpha = 1/3$  plateau region for the largest  $\epsilon_r$ ; however, this is not observed. Instead the local scaling exponent for largest  $\epsilon_r$  is generally very small in the range  $r > \lambda$ , suggesting that the second RSH may not apply for very high  $\epsilon_r$ . There is evidence, for example, that the local regions of highest dissipation rate are those kinematically related to regions of high vorticity gradient surrounding the strongest vortex tubes (Ashurst *et al.* 1987; Ruetsch & Maxey 1991; Lin 1993). If this is the case, the highest- $\epsilon_r$  regions would scale with the diameter of the vortex tubes, which themselves scale on the Kolmogorov scale  $\eta$  (Jimenez *et al.* 1993). Consequently, the characteristic scale for the highest- $\epsilon_r$  fluctuations (at any  $r$ ) would be the Kolmogorov scale,  $\eta$ , and an inertial-range scaling would be inappropriate.

#### 4.2. Scaling exponent over $r$

Now we examine the scaling relationship between  $\overline{\delta_r u | \epsilon_r}$  and the local length scale  $r$ , as indicated by equation (1.9). To illustrate, consider the log-log plot in figure 13(a) of  $\overline{\delta_r u | \epsilon_r}$  against  $r$  for the 256<sup>3</sup> forced DNS field at  $Re_\lambda = 151$ , where each curve is for a fixed  $\epsilon_r$  value. Since we used 201 bins for  $\epsilon_r$ , there can be 201 such curves possible. Of these we choose 41 bins with bin numbers 1, 6, 11, ..., 201 and plot the 29 curves with at least 2000 samples per point in the conditionally averaged  $\overline{\delta_r u | \epsilon_r}$ ;  $\epsilon_r$  increases from the lower-most to the upper-most curves. The curves for very small and very large  $\epsilon_r$  do not cover a broad range of  $r$  due to lack of samples, reflecting a decrease in the probability density of  $\epsilon_r$  with  $r$  at both very large and very small  $\epsilon_r$ . Figure 13(a) shows that the local slope  $\theta$ , corresponding to the scaling exponent in

$$\overline{\delta_r u | \epsilon_r} \propto r^\theta, \quad (4.2)$$

is very close to 1.0 for small  $r$  and decreases with increasing  $r$ .

To examine better the scaling exponents, we average the 16 curves that extend over all  $r$  values, shown in figure 13(b). The local slope of this curve is plotted in 13(c). The expected value of the scaling exponent  $\theta$  based on a Taylor series expansion in the limit  $r/\eta \rightarrow 0$  is reached when  $r/\eta \approx 1$ . In general,  $\theta$  decreases with increasing  $r$ , with a weak plateau developing near  $\theta \approx 1/3$  for  $\lambda < r < L_f$ . This tendency is not

---

FIGURE 13. (a) Velocity increment conditioned on the locally averaged dissipation,  $\overline{\delta_r u | \epsilon_r}$ , against  $r$  on a log-log plot, for the 256<sup>3</sup> forced DNS field at  $Re_\lambda = 151$ . Each curve corresponds to a fixed  $\epsilon_r$ . Dash lines indicate slope of 1 and 1/3, respectively. (b) The averaged curve of  $\overline{\delta_r u | \epsilon_r}$  against  $r$  from (a), dash lines indicate slope of 1 and 1/3, respectively. (c) The scaling exponent  $\theta$ , obtained as the local slope in (b), as a function of  $r$ . The horizontal lines mark the levels 1 and 1/3.

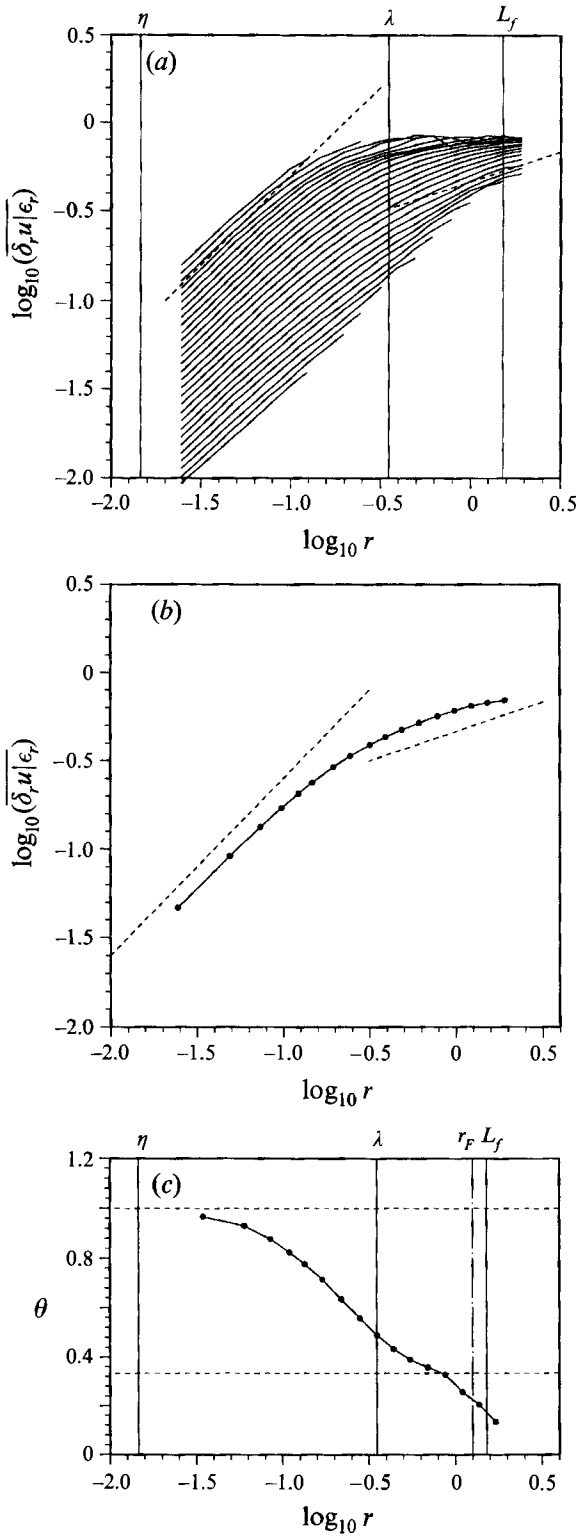


FIGURE 13. For caption see facing page.

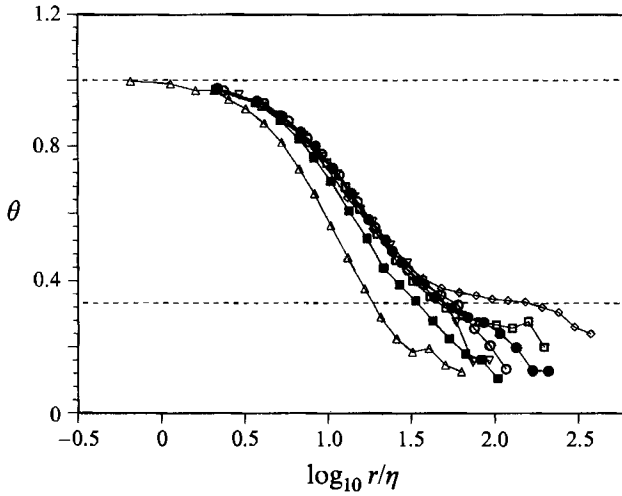


FIGURE 14. The scaling exponent  $\theta$  as a function of  $r/\eta$  for all the DNS simulation fields. The results for large-eddy simulation field are shown by  $\diamond$ , where the effective Kolmogorov scale is defined by the effective viscosity as given by equation (4.6).

strong because of the limited scale separation in the flow. When  $r \gtrsim L_f$ ,  $\theta$  decreases quickly towards zero.

A similar procedure was applied to all other flow fields; the DNS results are compiled in figure 14. Note in figure 14 that when  $r$  is scaled by  $\eta$  the scaling exponents collapse for  $R_\lambda \geq 100$  in the transition region,  $\theta = 1$  to  $\theta = 1/3$ . The level  $\theta = 1/3$  is first reached near  $\log_{10} r/\eta \approx 1.7$  or  $r/\eta \approx 50$ , and for the larger Reynolds numbers a weak plateau develops at  $\theta \approx 0.3$ . The over-resolved simulation at  $R_\lambda = 21$  shows clearly that  $\theta \rightarrow 1$  for  $r \rightarrow \eta$ . Also shown in figure 14 are the large-eddy simulation results. Although the plateau is marginal for the DNS fields at the highest Reynolds numbers owing to the limited scale separation, the LES field shows a plateau near  $\theta = 1/3$  for  $1.8 < \log_{10} r/\eta_e < 2.3$  or  $63 < r/\eta_e < 200$ , where the estimation of the effective Kolmogorov scale  $\eta_e$  is discussed in §4.3.

#### 4.3. Dependence on $R_\epsilon$ and universal constants

We end the discussions by analysing the *first* RSH using the two forced DNS fields at the highest  $R_\lambda$ , and the LES field. In addition, we briefly examine the Kolmogorov scalings for  $\overline{(\delta_r u)^n | \epsilon_r}$ , with  $n = 1, 2, 3, \dots, 8$  where, according to equation (1.7), the normalized moments

$$\frac{\overline{(\delta_r u)^n | \epsilon_r}}{(\epsilon_r r)^{n/3}}, \quad (4.3)$$

are a function only of  $R_\epsilon = \epsilon_r^{1/3} r^{4/3} / \nu$ . In figure 15(a) we replot the curves of figure 10(a) (256<sup>3</sup> forced DNS with  $R_\lambda = 151$ ) based on the first RSH. Several interesting observations can be made. First, the curves in figure 10 collapse reasonably well in figure 15(a), indicating that the first RSH, equation (1.7), provides a reasonable description for the conditionally averaged velocity increments. Second, the local Reynolds number  $R_\epsilon$  extends over about three and half decades, from 0.5 to over 1000, much larger than the length-scale separation in  $r$ , which is less than two decades (e.g. figure 10b). Third, based on a Taylor series expansion for  $r \rightarrow 0$ , for small  $R_\epsilon$ ,

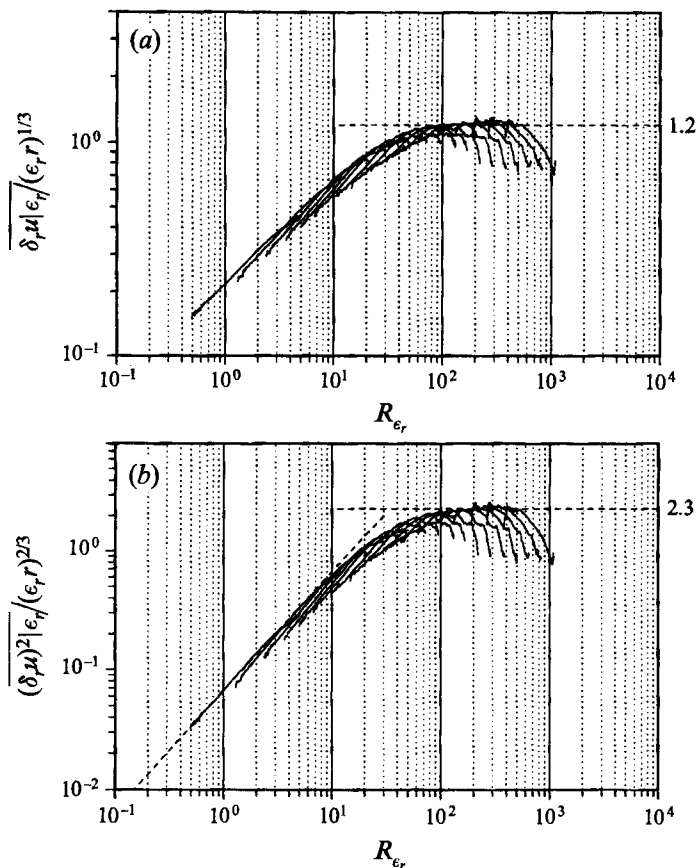


FIGURE 15. The dimensionless velocity increments  $(\delta_r u)^n | \epsilon_r / (\epsilon_r r)^{n/3}$  against the local Reynolds number  $Re_{\epsilon_r}$  for the  $256^3$  DNS field at  $Re_\lambda = 151$ . (a)  $n = 1$ , this is essentially a replot of figure 10(a); (b)  $n = 2$ , the relation  $(\delta_r u^2 | \epsilon_r) / (\epsilon_r r)^{2/3} = Re_{\epsilon_r} / 15$  is shown as a dash line.

the Reynolds number dependence should be

$$g_n(Re_{\epsilon_r}) \propto Re_{\epsilon_r}^{n/2}. \quad (4.4)$$

For  $n = 1$ , the slope should be 0.5, which is the case from figure 15(a) for  $Re_{\epsilon_r} \lesssim 10$ .

Most interestingly, those portions of the curves in figure 10(a) where the slope  $\alpha \approx 1/3$  are now connected together in figure 15(a) to give a plateau region for  $Re_{\epsilon_r} \gtrsim 100$ . This plateau region is expected if the second RSH, equation (1.9), applies. These results suggest that  $Re_{\epsilon_r} \gtrsim 100$  is sufficient for application of the second RSH. Furthermore, the level of the plateau provides an estimate for the universal constant  $D_1$  in equation (1.9). Shown as a dashed line,  $D_1 \approx 1.2 \pm 0.1$ . The results for  $n = 2$ , using the same flow field, are shown in figure 15(b), with the same overall characteristics as figure 15(a). The small- $Re_{\epsilon_r}$  limit can be derived analytically in the limit  $r \rightarrow 0$  to yield

$$g_2(Re_{\epsilon_r}) = \frac{Re_{\epsilon_r}}{15}. \quad (4.5)$$

This dependence is shown in figure 15(b) and matches well the region of  $Re_{\epsilon_r} < 10$ . The universal constant in the second RSH is  $D_2 = 2.3 \pm 0.2$ .

Figure 16 shows similar results for the  $512^3$  forced DNS field at  $R_\lambda = 195$ . The overall features are similar to figure 15, but with a slightly wider plateau yielding  $D_1 = 1.2 \pm 0.1$  and  $D_2 = 2.2 \pm 0.2$ . These values compare well with the  $R_\lambda = 151$  forced flow of figure 15.

As noted in §1, because the local Reynolds number of K62,  $Re_\epsilon = \epsilon_r^{1/3} r^{4/3} / \nu$ , spans a finite range at a given scale  $r$  as compared to a single value for the local Reynolds number  $R_r = \bar{\epsilon}^{1/3} r^{4/3} / \nu$  in K41, the inertial range in K62 context can be better realized than K41 for a given turbulence field at moderate Taylor microscale (global) Reynolds number  $R_\lambda$ . In other words, even for  $r$  close to the Kolmogorov scale  $\eta$ , it is possible, according to K62, to find sub-regions in the flow field where the K62 local Reynolds number  $Re_\epsilon$  is large and K62 inertial behaviour is realized. To demonstrate this, we plot  $\overline{\delta_r u} / (\bar{\epsilon} r)^{1/3}$  against  $R_r$  in figure 16(c) for the  $512^3$  simulation. A K41 inertial subrange would give a plateau region in figure 16(c). A comparison of figure 16(b) with figure 16(c) shows that universal constants ( $D_n$ ) in the second refined similarity hypothesis can be better determined than universal constants ( $B_n$ ) in K41. Further implications of the *wider* K62 inertial subrange for a given flow field will be discussed in a later paper.

To construct a similar K62 plot using the LES field, we introduce an effective viscosity  $\nu_e$ . A first choice is to use equation (3.7). By using  $\bar{\epsilon} = 0.1856$  (table 1),  $C_K = 1.532$  (see §2),  $k_c = 120.5$ , we obtain  $\nu_e = 0.000317$ . However, this value underestimates the true average effective viscosity, since it is known that the eddy viscosity has a cusp near the filter cut-off (Kraichnan 1976). A better way is to use the ensemble-averaged form of equation (3.5),

$$\nu_e \equiv \frac{\overline{F^d}}{2\overline{\delta_{ij}\delta_{ij}}} = \frac{\bar{\epsilon}}{2\overline{\delta_{ij}\delta_{ij}}}. \quad (4.6)$$

The average variance of the resolved strain rate is found to be  $\overline{\delta_{ij}\delta_{ij}} = 214$ . It follows that  $\nu_e = 0.000434$ . Using this effective viscosity and

$$\epsilon_r = F_r^d; \quad Re_{\epsilon_r} = \frac{\epsilon_r^{1/3} r^{4/3}}{\nu_e}, \quad (4.7)$$

where  $F_r^d$  is the flux  $F^d$  averaged over  $r$ , we obtain figure 17. Interestingly, plateau regions for both the first and second moments of the normalized, conditionally averaged velocity increments appear, giving  $D_1 = 1.2 \pm 0.1$  and  $D_2 = 2.3 \pm 0.2$ , *exactly* the same values as for the DNS flow fields.

We have also examined the third and fourth moments using the  $512^3$  forced DNS field at  $R_\lambda = 195$ . The overall dependence is similar to the case of  $n = 1$  but with a less well-defined plateau, giving  $D_3 = 5.0 \pm 0.5$  and  $D_4 = 14.0 \pm 1.0$ . The same third and fourth moment universal constants are found for the  $256^3$  DNS field at  $R_\lambda = 151$ , and for the LES field. We also computed the moments for  $n = 5, 6, 7$ , and 8 and estimated the corresponding universal constants. The results are:  $D_5 = 44.0 \pm 4.0$ ,  $D_6 = 150 \pm 15$ ,  $D_7 = 600 \pm 50$ , and  $D_8 = 2500 \pm 200$ . Both the general shape of  $g_n(Re_{\epsilon_r})$  at these orders and the constants  $D_n$  are the same for these flows. Clearly the  $D_n$  are no longer of order one for large  $n$ .

There is an alternative, straightforward way to estimate the universal constants  $D_n$ . According to the second RSH, the probability distribution of

$$\beta \equiv \frac{\delta_r u}{(\epsilon_r r)^{1/3}}, \quad (4.8)$$

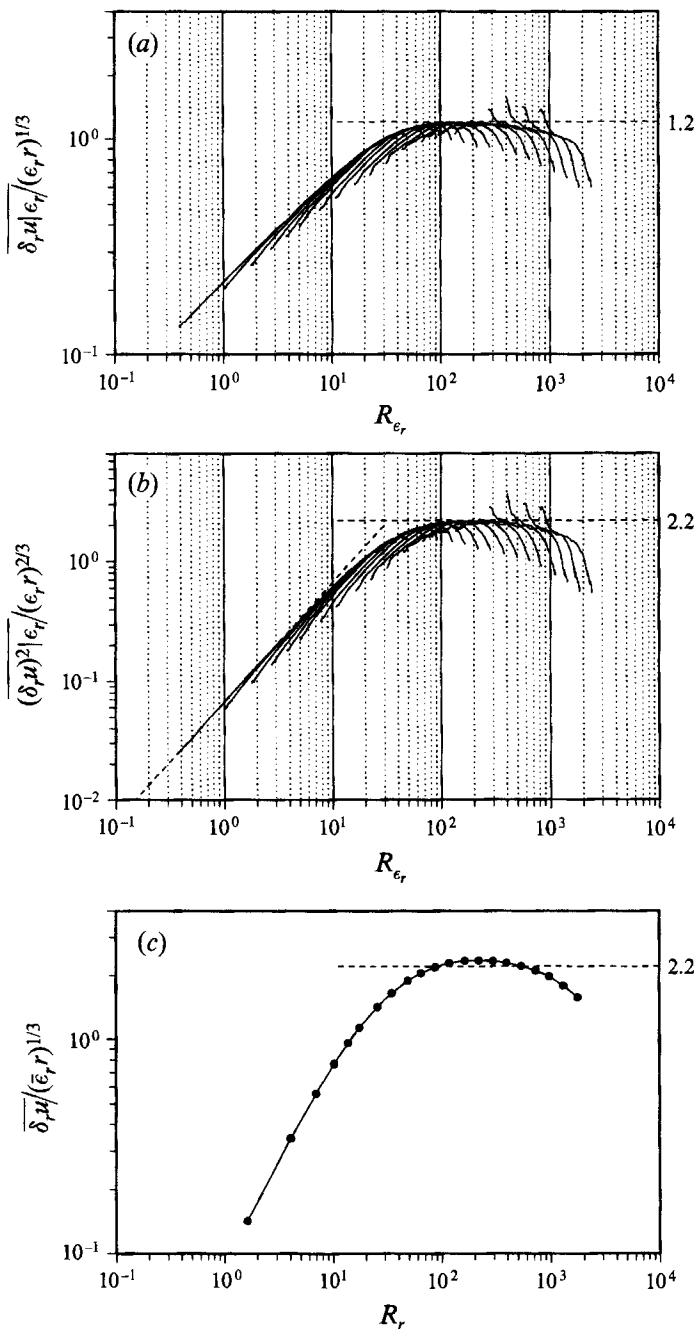


FIGURE 16. The dimensionless velocity increments  $\overline{|\delta_r u|^n} / (\epsilon_r r)^{n/3}$  against the local Reynolds number  $Re_{\epsilon_r}$  for the  $512^3$  DNS field at  $Re_\lambda = 195$ . (a)  $n = 1$ , this is essentially a replot of figure 11; (b)  $n = 2$ , the relation  $\overline{|\delta_r u|^2} / (\epsilon_r r)^{2/3} = Re_{\epsilon_r} / 15$  is shown as a dash line. (c)  $\overline{|\delta_r u|} / (\bar{\epsilon} r)^{1/3}$  against the K41 Reynolds number  $R_r$  for the same flow field.

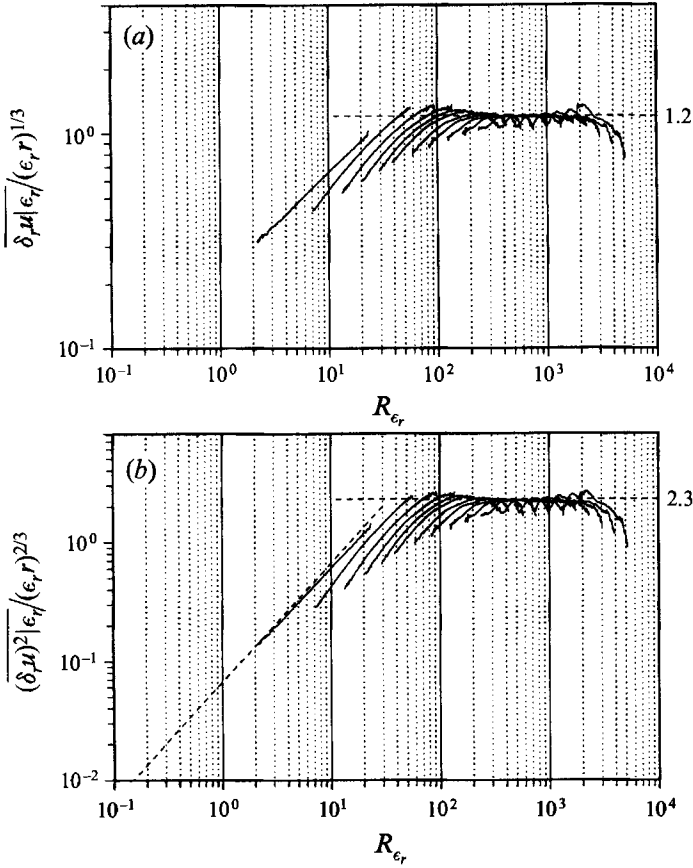


FIGURE 17. The dimensionless velocity increments  $\overline{(\delta_r u)^n} | \epsilon_r / (\epsilon_r r)^{n/3}$  against the local Reynolds number  $Re_{\epsilon_r}$  for the  $256^3$  LES field. (a)  $n = 1$ , this is essentially a replot of figure 12; (b)  $n = 2$ , the relation  $\overline{(\delta_r u)^2} | \epsilon_r / (\epsilon_r r)^{2/3} = Re_{\epsilon_r} / 15$  is shown as a dashed line.

$f(\beta)$ , is universal in the plateau regions of figures 15 to 17. The universal constants are then given as

$$D_n = \int_0^\infty \beta^n f(\beta) d\beta. \quad (4.9)$$

We computed  $f(\beta)$  based on a small selected  $(\epsilon_r, r)$  domain that forms a part of the plateau regions in figures 15 to 17. Figure 18 shows the probability distributions on logarithmic scales. The selected domain is  $r = 40\Delta$  and  $-2 < s_r < 0$  for the  $256^3$  forced DNS flow,  $r = 50\Delta$  and  $-1 < s_r < 1$  for the  $512^3$  forced DNS flow, and  $r = 16\Delta$  and  $-1 < s_r < 1$  for the LES flow field. Many other domains that form the plateau can be used if a more accurate  $f(\beta)$  is desired. Figure 18 indicates that the distribution is almost the same for the three cases, supporting the universality of the distribution. The discrepancy at large  $\beta$  may be due to statistical variability. Stolovitzky *et al.* (1992) recently measured the p.d.f. of  $\beta' \equiv \Delta_r u | \epsilon_r / (\epsilon_r r)^{1/3}$  in the inertial subrange, where  $\Delta_r u = u(x+r, y, z, t) - u(x, y, z, t)$ . The p.d.f. of  $\beta'$  should be closely related to the p.d.f. of  $\beta$  studied here. Stolovitzky *et al.* only showed the p.d.f. of  $\beta'$  for  $|\beta'| < 4$  and observed that it is close to Gaussian. The p.d.f. of  $\beta$  in figure 18 compares reasonably well with the Gaussian distribution, in good agreement with the



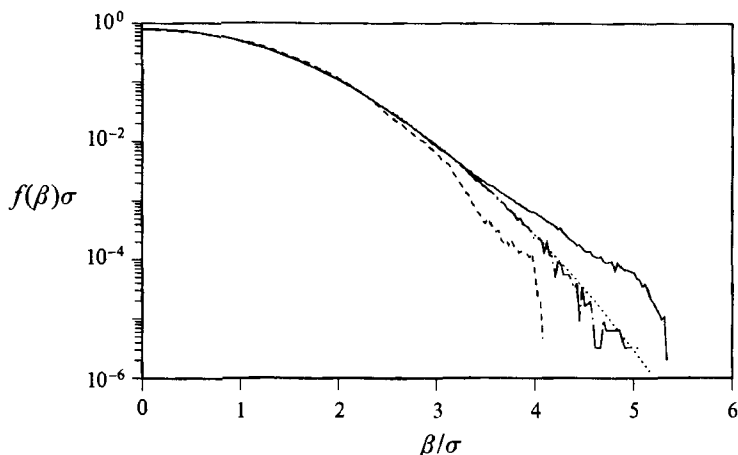


FIGURE 18. The probability distribution of  $\beta$  normalized by its standard deviation in the inertial subrange in the context of K62 on a log scale for three different flow fields: the  $256^3$  forced DNS flow (dashed line), the  $512^3$  forced DNS flow (solid line), and the LES field (chain-dotted line). The dotted line shows the Gaussian distribution.

results of Stolovitzky *et al.* The tail of the distribution shows some tendency of being exponential for the  $512^3$  simulation where enough samples are available to obtain an accurate result in the tail. It is not clear to us at the moment whether the tail will in fact be exponential at very large Reynolds numbers.

We now show that for the moments of  $\beta$ , the Gaussian distribution serves as a good model. In fact, if we assume that  $f(\beta)$  is given as

$$f(\beta) = \frac{2}{(2\pi)^{1/2}\sigma} \exp\left(-\frac{\beta^2}{2\sigma^2}\right), \quad (4.10)$$

where  $\sigma^2 = \int_0^\infty \beta^2 f(\beta) d\beta = D_2$ , we can obtain

$$D_n = \begin{cases} (n-1)!!\sigma^n & \text{for } n = 2, 4, 6, \dots; \\ (n-1)!!(2/\pi)^{1/2}\sigma^n & \text{for } n = 1, 3, 5, \dots \end{cases} \quad (4.11)$$

Based on the probability function, we obtain the value of  $D_n$  through equation (4.9) for the three fields. The results by this alternative method are presented in figure 19.

Also shown are the values and error bars obtained from the first method. They compare extremely well, indicating that the probability distribution in figure 18 is reasonably accurate. Of significance is the fact that  $D_n$  increases with  $n$  at a *faster-than-exponential* rate, which is also seen by the Gaussian model (4.11). Also shown in the figure by the dotted line is the Gaussian model (4.11). Figure 19 indicates that the Gaussian model works well for all  $n$ .

As a side note, figure 19 demonstrates that moments up to order 10 are reasonably well computed here. We have also checked this by plotting  $\beta^{10}f(\beta)$  against  $\beta$  and found that the peak is outside (to the left of) the noisy region of the curve.

To end this section we confirm that the RSH do not apply to the conditionally averaged velocity difference  $\underline{\Delta_r u}|\epsilon_r$ , without absolute sign, as noted in §1. Figure 20 shows the magnitude of  $\underline{\Delta_r u}|\epsilon_r$  against  $\epsilon_r$ , on a log-log plot similar to figure 10(a), for the  $256^3$  forced DNS flow field. There are about 201 data points for each curve. The two curves are for  $r = \Delta$  and  $r = 62\Delta$  respectively. Since  $\underline{\Delta_r u}|\epsilon_r$  can take both positive and negative values, we denote by symbols those data points (out of 201)

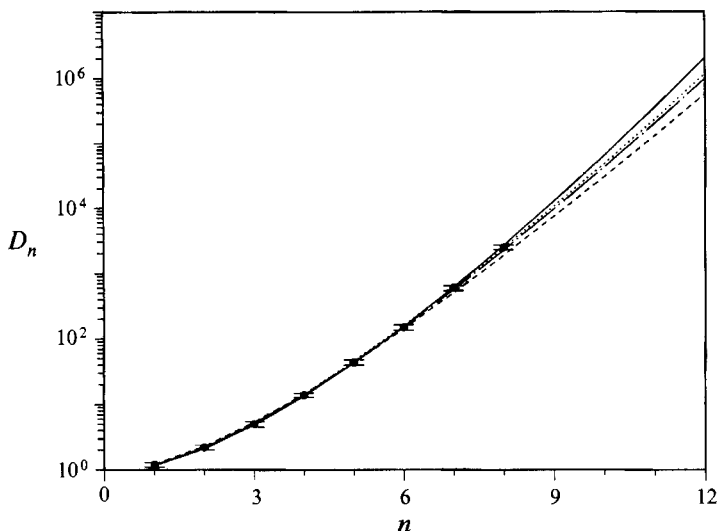


FIGURE 19. The universal constants  $D_n$  based on the probability distributions of  $\beta$  shown in figure 18 for the three different flow fields (line captions are the same as figure 18). Symbols are values determined from figures 15 to 17. The dotted line is the analytical expression based on the Gaussian model, equation (4.11).

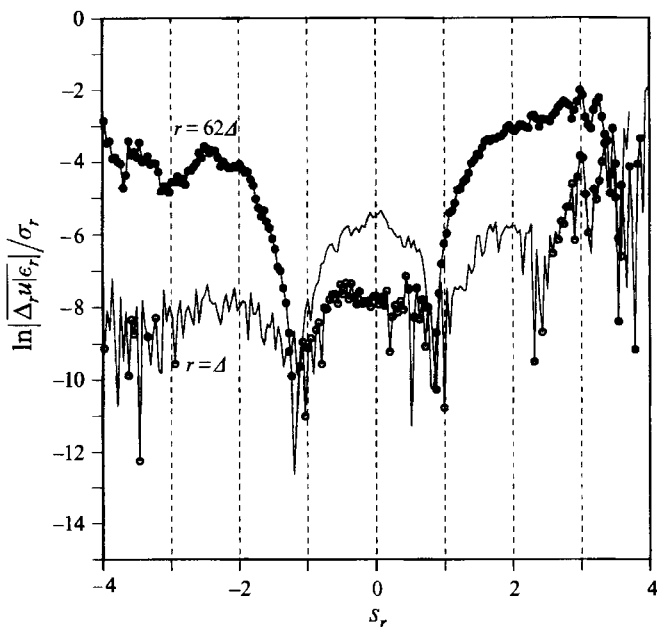


FIGURE 20. The magnitude of average velocity difference conditioned on  $\epsilon_r$ ,  $|\overline{\Delta_r u}|_{\epsilon_r}$  as a function of  $\epsilon_r$ , for the  $256^3$  forced DNS flow at  $r = \Delta$  and  $r = 62\Delta$ . The symbols (solid circles for  $r = \Delta$  and the open circles for  $r = 62\Delta$ ) mark the regions where  $\overline{\Delta_r u}|_{\epsilon_r}$  is positive, and the rest (unmarked) are the regions where  $\overline{\Delta_r u}|_{\epsilon_r}$  is negative. This plot should be compared with figure 10(a) for  $\overline{\delta_r u}|_{\epsilon_r}$ .

where  $\overline{\Delta_r u|\epsilon_r}$  is positive. It is evident that  $\overline{\Delta_r u|\epsilon_r}$  fluctuates around zero and there is no indication of power-law scaling.

To summarize, we have demonstrated in this section that the RSH provides a reasonable description for the conditionally averaged velocity increments when  $R_{\epsilon_r} > 100$ . The second RSH is supported quantitatively in terms of both the scaling exponents and universal constants in our high-resolution numerical turbulence fields. The universal constants are computed and are found to increase with the order  $n$  at a faster-than-exponential rate. Minor departures from the RSH for large- $\epsilon_r$  regions are noted, although more evidence is needed to confirm if such departures persist to higher Reynolds numbers.

## 5. The use of pseudo-dissipation in the study of the K62 theory

Most experimental studies of the K62 theory replace the actual dissipation rate  $\epsilon$  with the ‘pseudo’-dissipation rate  $\epsilon' = 15\nu(\partial u/\partial x)^2$ , which gives dissipation rate in an ensemble-average sense but not locally. Experimentally  $\epsilon'$  can be obtained by a single hot wire and Taylor’s frozen-field hypothesis while measurement of the full dissipation rate requires very sophisticated instrumentation (Champagne 1978; Tsinober *et al.* 1992; Wallace & Foss 1994). In this section, we analyse the similarities and differences of the two variables  $\epsilon$  and  $\epsilon'$  in context with the K62 theory.

### 5.1. Probability distribution

Compare first the distribution of the local, pseudo-dissipation rate  $\epsilon'$  given in figure 21 with the actual dissipation rate given in figure 5 for the same three flow fields (where the actual flux  $F^A$  is replaced by the ‘pseudo’-flux  $F'^A$  in the LES simulation). Although similarities between the signals are apparent, there are many differences as well. The distributions of  $\epsilon'$  in figure 21 are clearly more intermittent than those in figure 5. Although the mean of  $\epsilon'$  is equal to that of  $\epsilon$ , both the number of significant peaks and the peak magnitudes are larger in  $\epsilon'$  and the background level of  $\epsilon'$  is lower than  $\epsilon$ . These differences can be qualitatively explained by the full dissipation involving all nine different velocity derivatives in  $s_{ij}$ , while  $\epsilon'$  involves only one. The full dissipation  $\epsilon$  can be viewed roughly as an average of nine intermittent structures, each of which is like  $\epsilon'$ ; this averaging tends to reduce the degree of intermittency. Regions of extremely large  $\epsilon'$  tend to correspond to regions of large  $\epsilon$ , but not vice versa.

Figure 22 displays the probability distribution of  $\ln \epsilon'_r$  at four different  $r$  for the  $256^3$  forced DNS flow, for comparison with figure 6 for  $\ln \epsilon_r$ . The local averaging of  $\epsilon'_r$  is done in the same way as for  $\epsilon_r$  (see §3), which gives  $\epsilon'_r = \epsilon'$  when  $r = \Delta$ . The normalized logarithmic pseudo-dissipation is defined as  $s'_r \equiv (\ln \epsilon'_r - m'_r)/\sigma'_r$  with  $m'_r$  and  $\sigma'_r$  being the mean and standard deviation of  $\ln \epsilon'_r$ , respectively. Overall, there are significant differences between the p.d.f.s of  $\ln \epsilon_r$  and  $\ln \epsilon'_r$ . Consider first the probability distribution of  $\ln \epsilon' \equiv \ln \epsilon'_{r=\Delta}$ , given by the lowest curve in figure 22. This distribution is very different both from the Gaussian distribution and from the distribution of  $\ln \epsilon$ . It is strongly skewed, with a skewness of  $-1.34$  for  $s'$  as compared with  $-0.15$  for  $s$ . The probability distribution is linear for  $s' < -1$  on this log-scale plot. The linear variation between the logarithm of the p.d.f. and  $s'$  for  $s' \lesssim -1$  corresponds to the square-root singularity in the probability distribution of  $\epsilon'$  as noted by Narasimha (1990):

$$f(\epsilon') \propto \frac{1}{\epsilon'^{1/2}} \quad \text{as } \epsilon' \rightarrow 0. \quad (5.1)$$

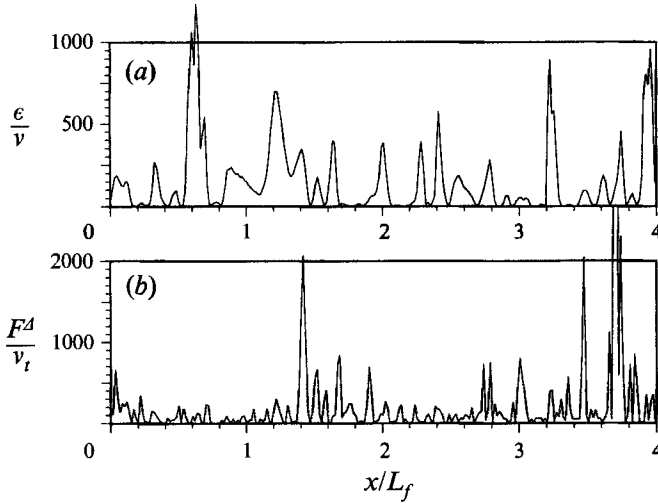


FIGURE 21. The local pseudo-dissipation rate (DNS) or modelled energy flux (LES) on a line  $y = z = L_B/2$  of length 4 integral length scales in the simulation box. (a) f256,  $Re_\lambda = 151$ ; (b) les256.

Combining (5.1) with (3.8) (where  $\epsilon$  is replaced by  $\epsilon'$ ), we obtain

$$f(s'_r) \propto \exp(\frac{1}{2}\sigma'^2 s'_r) \quad \text{as } s'_r \rightarrow -\infty, \quad (5.2)$$

giving a slope  $(\sigma' \log_{10} e)/2$  shown in figure 22 by the chain-dotted line and comparing very well to the actual slope. Because of this exponential tail, the flatness of  $s'$  is a rather high 6.4, as compared with 3.1 for  $s$ . For  $r > \Delta$ , the departures from Gaussianity are less severe, but always noticeable. Although the relative degree of the departures from Gaussianity of  $s'$  seems to reduce as  $r$  increases like  $s$  (figure 6), the p.d.f.s of  $s$  and  $s'$  are significantly different at all  $r$ . Note that the square-root singularity disappears as  $r$  increases and although the probability distributions for  $\epsilon_r$  and  $\epsilon'_r$  are very different for small  $r$ , both distributions tend to be closer to log-normal at large  $r$  values. Comparing figure 22 with figure 6 indicates that the distributions of  $\epsilon_r$  fluctuations are much closer to log-normal than  $\epsilon'_r$  at larger  $r$ .

The dependence of the variance  $\sigma_r'^2$  on  $r$  is shown in figure 23 for three representative flow fields for comparison with  $\sigma_r^2$  in figure 9. The maximum  $\sigma_r'^2$  is roughly five times larger than the maximum  $\sigma_r^2$  of about 1.1 in figure 9, consistent with the much higher level of intermittency in  $\epsilon'$  (figure 21). The variance  $\sigma_r'^2$  drops very quickly with increasing  $r$  with a characteristic much different from  $\sigma_r^2$  (figure 9). At the largest  $r$ , the two variances,  $\sigma_r'^2$  and  $\sigma_r^2$ , are not much different, with a value around  $0.2 \sim 0.3$ . The two variances should both approach zero for  $r \gg L_f$ . Consequently the corresponding intermittency parameter  $\mu'$  is larger than  $\mu$  in the inertial subrange for a finite Reynolds number flow. From figure 23, we obtain  $\mu' \sim 0.34$  for the DNS flows and  $\mu' \sim 0.25$  for the LES flow field. They are about 20% to 25% larger than the respective value for the full dissipation (§3). We note that the slope  $\mu'$  for DNS flows is not as well defined as  $\mu$ ; the value  $\mu'$  here is based on the region where  $r$  is relatively large and lies in the narrow inertial subrange, while a much wider range of  $r$  is used for  $\mu$ .

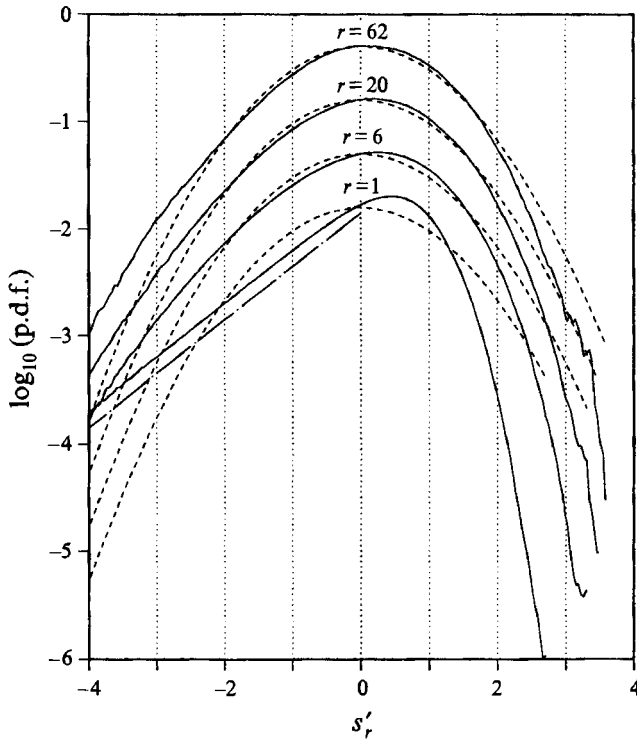


FIGURE 22. Probability density function of the logarithmic pseudo-dissipation,  $\ln \epsilon'_r$ , at four different  $r$  of 1, 6, 20, 62 grid spacings for the forced DNS field at  $Re_\lambda = 151$ . The curves are shifted by different amounts for  $r > 4$ . The dashed lines represent the Gaussian distribution.

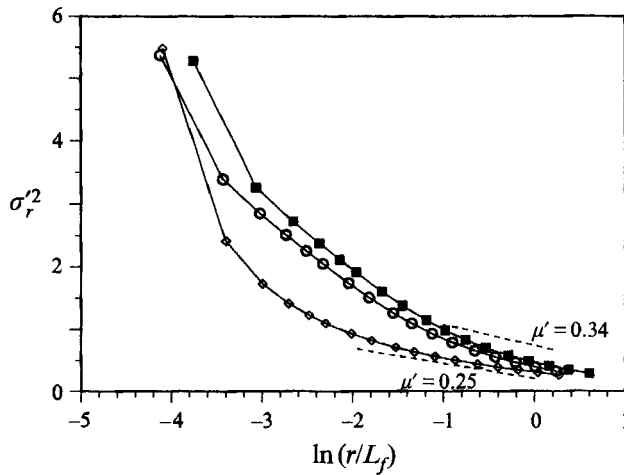


FIGURE 23. The variance of  $\ln \epsilon'_r$  against  $\ln r$  for the three flow fields: ■,  $256^3$ , free-decaying turbulence at  $Re_\lambda = 68.1$ ; ○,  $256^3$ , forced stationary turbulence at  $Re_\lambda = 151$ ; ◇,  $256^3$ , large-eddy simulation.

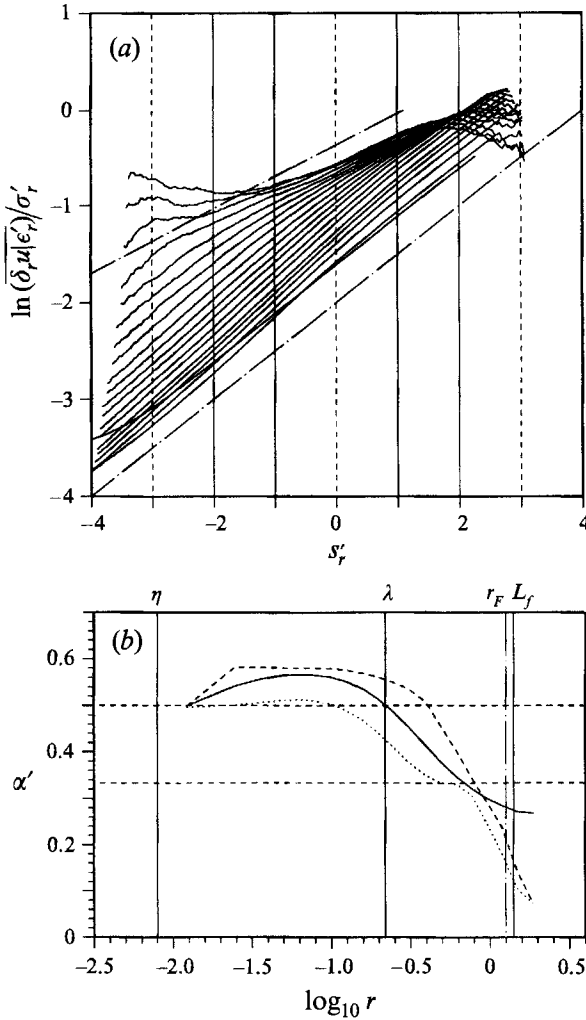


FIGURE 24. (a) Velocity increment conditioned on the locally averaged pseudo-dissipation,  $\overline{\delta_r u | \epsilon_r'}$ , against  $\epsilon_r'$  on a log-log plot, for the  $512^3$  forced DNS field at  $Re_\lambda = 195$ . Each curve corresponds to a fixed  $r$ , and from bottom to top,  $r$  changes from  $r_1 = \Delta = 1.5\eta$  to  $r_{20} = 152\Delta = 1.3L_f$ . (b) The power-law exponent  $\alpha'$  obtained as the average slope in (a) for the three regions  $-2 \leq s_r' < -1.0$  (dashed line),  $-1.0 \leq s_r' < 1.0$  (solid line), and  $1.0 \leq s_r' < 2$  (dotted line) as a function of  $r$ .

### 5.2. Refined similarity hypotheses

We now briefly compare the scaling exponent for  $\overline{\delta_r u | \epsilon_r'}$  with the scaling exponent for  $\overline{\delta_r u}$  discussed in §4. Figure 24(a) shows a log-log plot of  $\overline{\delta_r u | \epsilon_r'}$  against  $s_r'$ , for the  $512^3$  forced DNS field to be compared with figure 11(a) for  $\overline{\delta_r u | \epsilon_r}$  against  $s_r$  at different fixed  $r$ . The overall features of figures 24(a) and 11(a) are similar with three noticeable differences. The first difference is that the curves in figure 24(a) are shifted slightly to the left as a result of a much more strongly skewed distribution of  $\epsilon_r'$  compared with  $\epsilon_r$ . Secondly the  $\epsilon_r'$  curves cover a much narrower range in  $\overline{\delta_r u | \epsilon_r'}$  than do the  $\epsilon_r$  curves. Thirdly the  $\epsilon_r'$  curves at small- $r$  are not as well approximated by straight lines as are the small  $r$  values for  $\epsilon_r$  in figure 11(a). Indeed, this statement can be made about all curves in figure 24(a) as compared with 11(a).

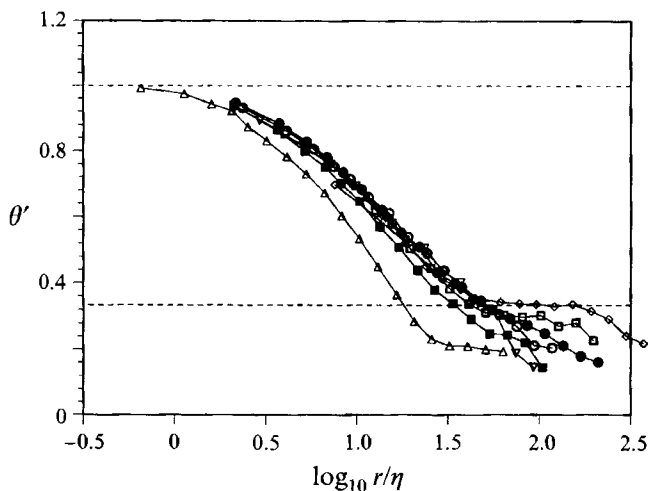


FIGURE 25. The scaling exponent  $\theta'$  as a function of  $r/\eta$  for all flow fields.

Figure 24(b) displays the scaling exponent  $\alpha'$  for some three subregions of  $s'_r$  as those chosen for  $s_r$  in figure 11(b). Similar to figure 11(b), there is a weak plateau of  $\alpha' = 1/3$  at scales between  $\lambda$  and  $L_f$  but occurring for  $1.0 \leq s'_r < 2.0$ , and the exponent decreases quickly as  $r$  increases beyond  $L_f$ . Although  $\alpha'$  approaches 0.5 as  $r \rightarrow \eta$  like  $\alpha$ , for  $\Delta < r < \lambda$ , the scaling exponents are significantly larger than 0.5 and depend more strongly on  $\epsilon'_r$  as compared with figure 11(b) for  $\alpha$ . This indicates that the power-law dependence is less well satisfied for  $\epsilon'_r$  than for  $\epsilon_r$ . Similar results are found for other flow fields.

The same postprocessing procedure as discussed in §4.2 for the scaling of  $\overline{\delta_r u | \epsilon_r}$  with  $r$  is applied here to obtain the scaling exponents of  $\overline{\delta_r u | \epsilon'_r}$  with  $r$ . The final results for all the seven flow fields under Kolmogorov scaling are shown in figure 25 for comparison with figure 14. As before, for the LES field we introduce an effective Kolmogorov scale  $\eta_e = (v_e^3 / \bar{\epsilon})^{1/4}$  based on the effective viscosity  $\nu_e$  defined by equation (4.6). The overall features of figure 25 are similar to figure 14. Interestingly, the data for the LES field also match those of the high Reynolds number DNS fields in the transition region. For the LES field, there is a well-defined  $\theta' = 1/3$  region starting from  $r/\eta_e \approx 50$ . Again the exponent becomes one as  $r/\eta \rightarrow 1$ .

While the difference in scaling exponents obtained by using  $\epsilon_r$  vs.  $\epsilon'_r$  is not severe, universality is not so well approximated using  $\epsilon'_r$ ; this is shown in figure 26, where the first and second moments are plotted against the local Reynolds number  $R_{\epsilon'_r} = \epsilon_r'^{1/3} r^{4/3} / \nu$ . Compared to figure 16, the curves in figure 26 show a lesser degree of collapse and little apparent plateau region for  $R_{\epsilon'_r} > 100$ . Indeed, without reference to figure 16, it would be difficult to extract the universal constants  $D_1$  and  $D_2$  from figure 26, although the levels based on figure 16 apply marginally in figure 26.

The comparison between  $F_r'^A$  and  $F_r^A$  for the LES field appears to be somewhat better (figure 27). Although the plateau regions are much narrower than in figure 17, they are clear enough to allow for an estimate of the universal constants  $D_1$  and  $D_2$ , which are the same as from figure 17 before.

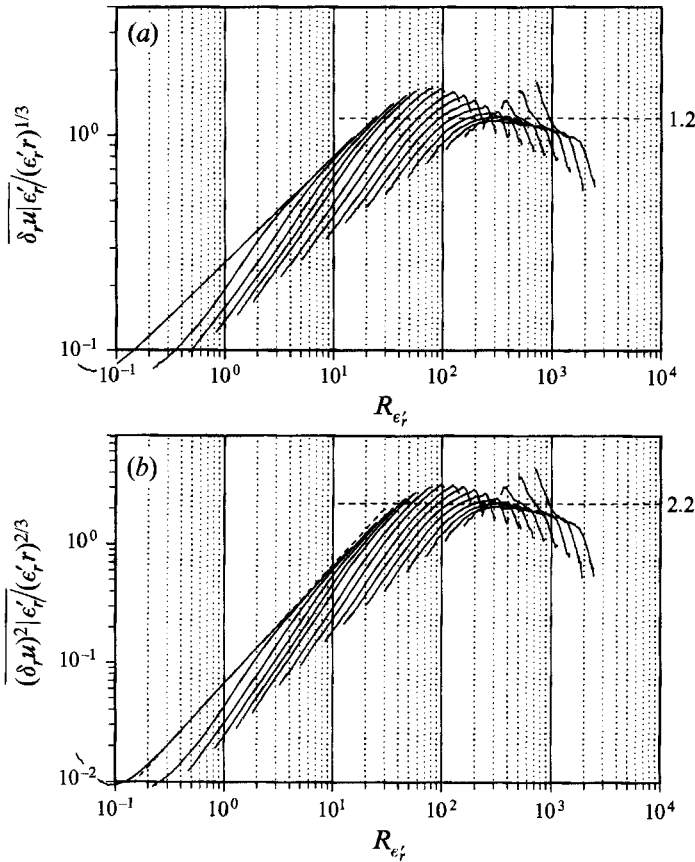


FIGURE 26. The dimensionless velocity increments  $(\delta_r u)^n / (\epsilon_r r)^{n/3}$  against the local Reynolds number  $Re_{\epsilon_r}$  for the  $512^3$  DNS field at  $Re_\lambda = 195$ . (a)  $n = 1$ , this is a replot of figure 11 using  $\epsilon_r'$ ; (b)  $n = 2$ . Note that the deviation for the smallest  $r$  from the relation  $(\delta_r u^2 / (\epsilon_r r)^{2/3}) / (\epsilon_r r)^{2/3} = Re_{\epsilon_r} / 15$  is a numerical artifact of adding a very small number when taking the logarithm of  $\epsilon_r'$ .

## 6. Concluding remarks

High-resolution direct Navier–Stokes simulations make it possible to generate instantaneous turbulence fields at moderate to high Reynolds numbers, with realistic small-scale features in both the inertial and dissipation subranges. These allow us to examine directly the fundamental hypotheses underlying Kolmogorov–Obukhov (1962) turbulence theory. Our analyses were motivated by recent work (Hosokawa & Yamamoto 1992; Chen *et al.* 1993) concerning the validity of these hypotheses, but are carried out in great quantitative detail to obtain scaling exponents and universal constants. We have demonstrated that the probability distribution of locally averaged dissipation rate  $\epsilon_r$  over a length scale  $r$  is nearly log-normal in the inertial subrange, but with significant departures in the tails. These departures play an important role in high-order moments of dissipation fluctuations. The intermittency parameter  $\mu$ , appearing in the Kolmogorov’s third hypothesis for the variance of the logarithmic dissipation, is found to be in the range of 0.20 to 0.28, in good agreement with recent experimental measurements based on pseudo-dissipation rate (Anselmet *et al.* 1984; Sreenivasan & Kailasnath 1993; Praskovsky & Oncley 1994) and numerical



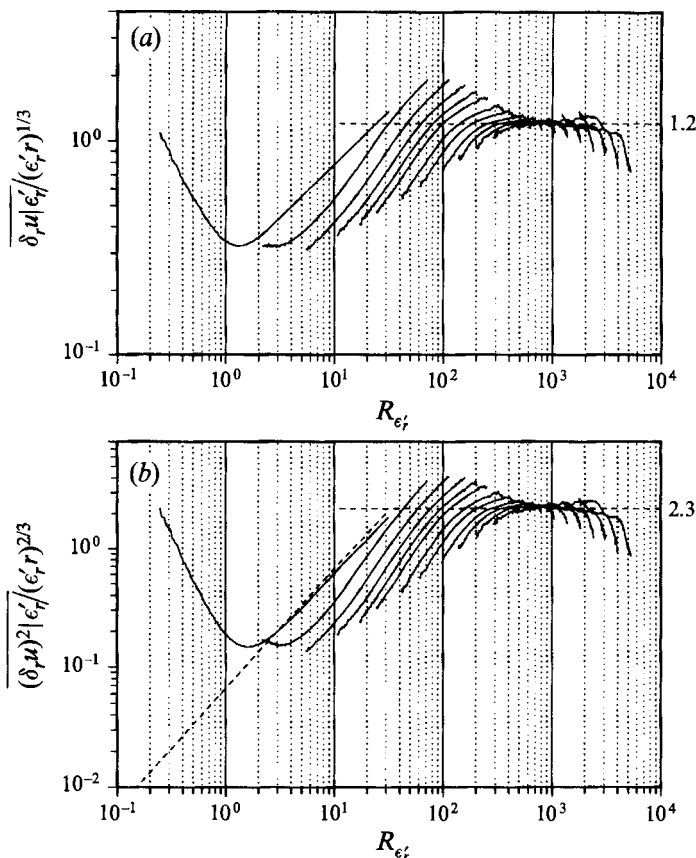


FIGURE 27. The dimensionless velocity increments  $\overline{(\delta_r u)^n | \epsilon_r^n / (\epsilon_r r)^{n/3}}$  against the local Reynolds number  $Re_{\epsilon_r}$  for the LES field. (a)  $n = 1$ , this is essentially a replot of figure 12 using  $\epsilon_r'$ ; (b)  $n = 2$ . Note that the deviation for the smallest  $r$  from the relation  $\overline{(\delta_r u)^2 | \epsilon_r^2} / (\epsilon_r r)^{2/3} = Re_{\epsilon_r} / 15$  is a numerical artifact of adding a very small number when taking the logarithm of  $\epsilon_r'$ .

simulations (Vincent & Meneguzzi 1991). The scaling exponents over both  $\epsilon_r$  and  $r$  for the conditionally averaged velocity increments  $\overline{\delta_r u | \epsilon_r}$  are quantified, which provide direct evidence in support of the refined similarity hypotheses. Even more directly, the dimensionless averaged velocity increments  $\overline{(\delta_r u^n | \epsilon_r)} / (\epsilon_r r)^{n/3}$  are found to depend on the local Reynolds number  $Re_{\epsilon_r} = \epsilon_r^{1/3} r^{4/3} / \nu$  in a manner consistent with the refined similarity hypotheses. In the inertial subrange, the probability distribution of  $\overline{\delta_r u | \epsilon_r} / (\epsilon_r r)^{1/3}$  is found to be nearly universal and is close to Gaussian distribution. Universal constants in the second RSH are determined quite accurately and found to increase with the order  $n$  at a faster-than-exponential rate.

Just as the log-normal model for the distribution of the dissipation-rate fluctuations has its limitations, the evidence we gather here indicates that the refined similarity hypotheses may not apply to regions of very large  $\epsilon_r$ . These departures are similar in the different simulated flows, and thus may persist to higher Reynolds number flows. Further studies are needed to clarify this observation.

The use of pseudo-dissipation, often employed in experimental work, is critically examined in the context of the K62 theory. We found that the probability distribution of locally averaged pseudo-dissipation  $\epsilon_r'$  deviates more from a log-normal model

than the full dissipation  $\epsilon_r$ , and the intermittency parameter  $\mu'$  based on the pseudo-dissipation can be larger than  $\mu$  based on the full dissipation in finite Reynolds number turbulence. The velocity increments conditioned on  $\epsilon'_r$  do not follow the refined similarity hypotheses to the same degree as those conditioned on  $\epsilon_r$ . Consequently, we anticipate that consistency with the refined similarity hypotheses will require higher Reynolds numbers using pseudo-dissipation than the full dissipation rate. We conclude that the actual dissipation rate is preferred to the pseudo-dissipation rate in the study of the K62 theory, particularly at moderate Reynolds numbers.

The results presented here are limited to moderate turbulence Reynolds numbers. One should not draw definitive conclusions based on existing DNS results. However, our results do give supportive evidence to the K62 theory. Direct numerical simulations at higher Reynolds numbers are needed to fully resolve the issues in K62. The large-eddy simulation flow field, in principle, provides a portion of the inertial subrange at infinite Reynolds number, but does not resolve the dissipation field directly; thus, approximations have to be made in furnishing the locally averaged dissipation field. Most experimental studies involve turbulence fields at much higher Reynolds numbers; however, they do not examine the hypotheses embedded in the K62 theory directly. In view of the significance of the refined similarity hypotheses and possible minor departures for regions of very high dissipation rate as noted in this study, it would be desirable for experimentalists to examine these hypotheses directly in a manner similar to this study. Experimental determination of the universal constants  $D_n$  in the second refined similarity hypothesis would also be useful.

We thank Gary D. Doolen for his help in the numerical simulations and Robert H. Kraichnan, Andrew Siegel, Gustavo Stolovitzky, and L. J. Peltier for useful discussions. Brian Moquin helped us to construct figure 4 of Three-dimensional visualization. L.P.W. is grateful to his friends in Los Alamos, particularly to Dongming Zhao and Shuling Hou, for making his visits to Los Alamos during the course of this work very pleasant. This work was supported by ARO/URI grant DAAL03-92-G-0117 (monitored by Dr Walter Bach), AFOSR/URI grant number AFOSR-90-0113 (monitored by Dr James McMichael), and the US Department of Energy through Los Alamos National Laboratory. The numerical simulations were performed on the CM-5 at the Advanced Computing Laboratory at Los Alamos National Laboratory.

#### REFERENCES

- ANSELMET, F., GAGNE, Y., HOPFINGER, E. & ANTONIA, R. A. 1984 High-order velocity structure functions in turbulent shear flows. *J. Fluid Mech.* **140**, 63–89.
- ANTONIA, R. A., SATYAPRAKASH, B. R. AND HUSSAIN, A. K. M. F. 1982 Statistics of fine-scale velocity in turbulent plane and circular jets. *J. Fluid Mech.* **119**, 55–89.
- ASHURST, W. T., KERSTEIN, A. R., KERR, R. M. & GIBSON, C. H. 1987 Alignment of vorticity and scalar gradient with strain in simulated Navier Stokes turbulence. *Phys. Fluids* **30**, 3243–3253.
- BRASSEUR, J. G. & CORRISIN, S. 1987 Spectral evolution of the Navier–Stokes equations for low order couplings of Fourier modes. In *Advances in Turbulence* (ed. G. Comte-Bellot & J. Mathieu), pp. 152–162. Springer.
- CHAMPAGNE, F. H. 1978 The fine-scale structure of turbulent velocity field. *J. Fluid Mech.* **86**, 67–108.
- CHEN, S., DOOLEN, G. D., KRAICHNAN, R. H. & SHE, Z.-S. 1993 On statistical correlations between velocity increments and locally averaged dissipation in homogeneous turbulence. *Phys. Fluids A* **5**, 458–463.
- CHEN, S. & SHAN X. 1992 High resolution turbulence simulations using the Connection Machine-2. *Comput. Phys.* **6**, 643.

- COMTE-BELLOT, G. & CORRISIN, S. 1971 Simple Eulerian time correlation of full- and narrow-band velocity signals in grid-generated, 'isotropic' turbulence. *J. Fluid Mech.* **48**, 273–337.
- ESWARAN, V. & POPE, S. B. 1988 An examination of forcing in direct numerical simulations of turbulence. *Computers Fluids* **16**, 257–278.
- GIBSON, C. H., STEGEN, G. R. & MCCONNELL, S. 1970 Measurements of the universal constant in Kolmogorov's third hypothesis for high Reynolds number turbulence. *Phys. Fluids* **13**, 2448–2451.
- GURVICH, A. S. & YAGLOM, A. M. 1967 Breakdown of eddies and probability distributions for small-scale turbulence. *Phys. Fluids Suppl.* S59–S65.
- HOSOKAWA, I. 1991 Temperature structure functions in isotropic turbulence. *Phys. Rev. A* **43**, 6735–6739.
- HOSOKAWA, I. & YAMAMOTO, K. 1992 Evidence against the Kolmogorov refined similarity hypothesis. *Phys. Fluids A* **4**, 457–459.
- JIMÉNEZ, J., WRAY, A. A., SAFFMAN, P. G. & ROGALLO R. S. 1993 The structure of intense vorticity in isotropic turbulence. *J. Fluid Mech.* **255**, 65–90.
- KERR, R. T. 1985 High-order derivative correlations and the alignment of small-scale structures in isotropic numerical turbulence. *J. Fluid Mech.* **153**, 31–58.
- KERR, R. T. 1990 Velocity, scalar and transfer spectra in numerical turbulence. *J. Fluid Mech.* **211**, 309–332.
- KIDA, S. 1991 Log-stable distribution in turbulence. *Fluid Dyn. Res.* **8**, 135–138.
- KOLMOGOROV, A. N. 1941a The local structure of turbulence in incompressible viscous fluid for very large Reynolds numbers. *C.R. Acad. Sci. URSS* **30**, 301–305.
- KOLMOGOROV, A. N. 1941b Dissipation of energy in the locally isotropic turbulence. *C.R. Acad. Sci. URSS* **32**, 16.
- KOLMOGOROV, A. N. 1962 A refinement of previous hypotheses concerning the local structure of turbulence in a viscous incompressible fluid at high Reynolds number. *J. Fluid Mech.* **13**, 82–85.
- KRAICHNAN, R. H. 1974 On Kolmogorov's inertial-range theories. *J. Fluid Mech.* **62**, 305–330.
- KRAICHNAN, R. H. 1976 Eddy viscosity in two and three dimensions. *J. Atmos. Sci.* **33**, 1521–1536.
- KUO, A. Y. S. & CORRISIN, S. 1971 Experiments on intermittency and fine-structure distribution functions in fully turbulent field. *J. Fluid Mech.* **50**, 285–319.
- LANDAU, L. E. & LIFSHITZ, E. M. 1963 *Fluid Mechanics*. p. 126, Pergamon.
- LEE, M. J. & REYNOLDS, W. C. 1985 Numerical experiments on the structure of homogeneous turbulence. *Department of Mechanical Engineering Rep.* TF-24 Stanford University, Stanford, CA.
- LIN, W.-Q. 1993 Structural and dynamical characteristics of intermittent structures in homogeneous turbulent shear flow. PhD Thesis, Department of Mechanical Engineering, Pennsylvania State University.
- LIU, T. 1993 A note on the probability distribution of the dissipation rate in locally isotropic turbulence. *Phys. Fluids A* **5**, 2234–2238.
- MANDELBROT, B. B. 1974 Intermittent turbulence in self-similar cascade: divergence of high moments and dimension of the carrier. *J. Fluid Mech.* **62**, 331–358.
- MENEVEAU, C., SREENIVASAN, K. R., KAILASNATH, P. & FAN, M. S. 1990 Joint multifractal measures: theory and applications to turbulence. *Phys. Rev. A* **41**, 894–913.
- MÉTAIS, O. & LESIEUR, M. 1992 Spectral large-eddy simulation of isotropic and stably stratified turbulence. *J. Fluid Mech.* **239**, 157–194.
- MONIN, A. S. & YAGLOM, A. M. 1975 *Statistical Fluid Mechanics, Mechanics of Turbulence*, Vol 2. MIT Press.
- NARASIMHA, R. 1990 The utility and drawback of traditional approaches. In *Whither Turbulence? Turbulence at the Crossroads* (ed. J. L. Lumley). Lecture Notes in Physics, Vol. 357. Springer.
- NOVIKOV, E. A. 1970 Intermittency and scale similarity of the structure of turbulent flow. *Prikl. Math. Mekh.* **35**, 266–277.
- OBOUKHOV, A. M. 1962 Some specific features of atmospheric turbulence. *J. Fluid Mech.* **13**, 77–81.
- PELTIER, L. J. & WYNGAARD, J. C. 1995 Mean and local structure-function parameters in the convective boundary layer from large-eddy simulation. *J. Atmos. Sci.* (to appear).
- PIOMELLI, U., CABOT, W. H., MOIN, P. & LEE, S. 1991 Subgrid-scale backscatter in turbulent and transitional flows. *Phys. Fluids A* **3**, 1766–1771.

- PRASKOVSKY, A. A. 1992 Experimental verification of the Kolmogorov refined similarity hypothesis. *Phys. Fluids A* **4**, 2589–2591.
- PRASKOVSKY, A. A. & ONCLEY, S. 1994 Measurements of the Kolmogorov constant and intermittency exponent at very high Reynolds numbers. *Phys. Fluids* **6**, 2886–2888.
- RUETSCH, G. R. & MAXEY, M. R. 1991 Small-scale features of vorticity and passive scalar fields in homogeneous isotropic turbulence. *Phys. Fluids A* **3**, 1587–1597.
- SHE, Z.-S., CHEN, S., DOOLEN, G., KRAICHNAN, R. H. & ORSZAG, S. A. 1993 Reynolds number dependence of isotropic Navier–Stokes turbulence. *Phys. Rev. Lett.* **70**, 3251–3254.
- SHE, Z.-S. & LEVEQUE, E. 1994 Universal scaling laws in fully developed turbulence. *Phys. Rev. Lett.* **72**, 336–339.
- SHE, Z.-S. & WAYMIRE, E. C. 1995 Quantized energy cascade and log-Poisson statistics in fully developed turbulence. *Phys. Rev. Lett.* **68**, 2762–2765.
- SREENIVASAN, K. R. 1984 On the scaling of the turbulence energy dissipation rate. *Phys. Fluids* **27**, 1048–1051.
- SREENIVASAN, K. R. & KAILASNATH, P. 1993 An update on the intermittency exponent in turbulence. *Phys. Fluids A* **5**, 512–514.
- STOLOVITZKY, G., KAILASNATH, P. & SREENIVASAN, K. R. 1992 Kolmogorov’s refined similarity hypotheses. *Phys. Rev. Lett* **69**, 1178–1181.
- STOLOVITZKY, G. & SREENIVASAN, K. R. 1993 Scaling of structure functions. *Phys. Rev. E* **48**, R33–36.
- STOLOVITZKY, G. & SREENIVASAN, K. R. 1994 Kolmogorov’s refined similarity hypotheses for turbulence and general stochastic processes. *Rev. Mod. Phys.* **66**, 229–240.
- THORODDSEN, S. T. & VAN ATTA, C. W. 1992 Experimental evidence supporting Kolmogorov’s refined similarity hypothesis. *Phys. Fluids A* **4**, 2592–2594.
- TSINOBER, A., KIT, E. & DRACOS, T. 1992 Experimental investigation of the field of velocity gradients in turbulent flows. *J. Fluid Mech.* **242**, 169–192.
- VAN ATTA, C. W. & ANTONIA, R. A. 1980 Reynolds number dependence of skewness and flatness factors of turbulent velocity derivatives. *Phys. Fluids* **23**, 252–257.
- VAN ATTA, C. W. & PARK, J. 1972 Statistical self-similarity and inertial subrange turbulence. In *Statistical models and Turbulence. Proc. Symp. at San Diego, July 15–21, 1971* (ed. M. Rosenblatt & C. Van Atta). Lecture Notes in Physics, Vol. 12, pp. 402–426. Springer.
- VINCENT, A. & MENEGUZZI, M. 1991 The spatial structure and statistical properties of homogeneous turbulence. *J. Fluid Mech.* **225**, 1–20.
- WALLACE, J. M. & FOSS, J. F. 1994 The measurement of vorticity in turbulent flows. *Ann. Rev. Fluid Mech.* **27**, 469–514.
- WYNGAARD, J. C. & PAO, Y. H. 1971 Some measurements of the fine structure of large Reynolds number turbulence. *Statistical models and Turbulence. In Proc. Symp. at San Diego, July 15–21, 1971* (ed. M. Rosenblatt & C. Van Atta). Lecture Notes in Physics, Vol. 12, pp. 384–401. Springer.
- WYNGAARD, J. C. & TENNEKES, H. 1970 Measurements of the small-scale structure of turbulence at moderate Reynolds numbers. *Phys. Fluids* **13**, 1962–1969.
- YEUNG, P. K. & BRASSEUR, J. G. 1991 The response of isotropic turbulence to isotropic and anisotropic forcing at the large scales. *Phys. Fluids A* **3**, 884–897.